UNIVERSITY OF CALIFORNIA,
IRVINE

Theoretical Modeling of Unsteady Aerodynamic Loads on Plunging Airfoils in a Subsonic Compressible Flow

THESIS

submitted in partial satisfaction of the requirements
for the degree of

MASTER OF SCIENCE

in Mechanical and Aerospace Engineering

by

Ahmed Ismail EL-Nadi

Thesis Committee:
Professor Haithem E.Taha, Chair
Professor Feng Liu
Professor Dimitri Papamoschou

2021

DEDICATION

This thesis is dedicated to

my parents

for their endless love and support. They were always by my side and helped me to get through tough times.

my wife

for loving me and for her patience and deep understanding.

TABLE OF CONTENTS

LIST OF FIGURES

LIST OF TABLES

Nomenclature

$a = \sqrt{\gamma p/\rho}$	Speed of sound.
b	Flat plate half chord.
c	Flat plate chord.
$C(K)$	Theodorsen function.
$\mathbf{g}$	Gravity vector.
$\overline{H} = \frac{H}{b}$	Non-dimensional plunging motion amplitude.
$\ddot{H}$	Plunging acceleration.
H_n^m	Hankel function of kind m and order n.
$K = \frac{\omega U}{b}$	Reduced Frequency.
$\kappa = \frac{KM}{1-M^2}$	Compressible reduced frequency.
K_{hf}	High frequency gain.
$\overline{L}$	Total aerodynamic lift amplitude.
$\overline{L}^{(1)}$	Non-circulatory lift amplitude.
$\overline{L}^{(2)}$	Circulatory lift amplitude.
$L(t)$	Total aerodynamic lift.
$\hat{L_{\overline{H}}}$	Total lift in a complex form.
L_{QS}	Plunging motion quasi-steady lift.
$L_{C,\overline{H}}$	Circulatory lift due to plunging.
$L_{NC,\overline{H}}$	Non-circulatory lift due to plunging motion
$M = \frac{U}{a}$	Free stream Mach number.
P_t	Total pressure.
P_o	Free stream pressure.
$\overline{P}(x)$	Local pressure magnitude.
$p,\ \rho$	Perturbation pressure and density, respectively.

Q	Elliptic coordinates semi-focal length.
q	$\frac{Q^2\kappa^2}{4}$.
R	Kernel function.
r	$\sqrt{X^2+Y^2+Z^2}$.
u_t, v_t and w_t	Total velocity components.
$u,\ v$ and w	Perturbation velocity components.
U	Free stream velocity in x-direction.
$\mathbf{V}_t$	Total velocity vector.
$W''(x,y,t)$	Airfoil downwash.
$\overline{W''}$	Downwash magnitude.
x, y, z, χ and η	Cartesian coordinates.
x^*	$\frac{x}{2b}$.
$X=\frac{x}{b}, Y=\frac{y}{b}$ and $Z=\frac{\beta z}{b}$	Non-dimensional Cartesian coordinates.
$ce_m,\ se_m$	Cosine elliptic and sine elliptic angular Mathieu functions, respectively, of order m.
$Mc_i^{(j)},\ Ms_i^{(j)}$	Radial Mathieu functions of kind j and order i
ρ_t	Total fluid density.
ρ_o	Free stream fluid density.
ϕ_t	Total velocity potential.
ϕ	Perturbation velocity potential.
μ^*	Dynamic viscosity.
$\boldsymbol{\tau}$	Viscous stress tensor.
$\boldsymbol{\Omega}$	Vorticity vector.
Γ	Circulation.
γ_b	Bound vortex.
γ	Specific heat ratio of gases.

α	Angle of attack.
σ	Angle between the normal to the airfoil surface and y and z directions.
ω	Radian frequency.
Φ	Acceleration potential.
θ	angle measured from airfoil mid-chord point
Π	Arbitrary function representing doublet intensity
ξ and ζ	Elliptic coordinate system.
β	$\sqrt{1-M^2}$
λ_a	Acoustics wavelength.
$\mu = \frac{KM^2}{1-M^2}$	Non-dimensional variable.
$\overline{\alpha}$	Pitching amplitude.

ACKNOWLEDGMENTS

I'd like to thank Professor Taha for his support and patience and for giving me the opportunity to finish this work. Professor. Taha is not just my Master's advisor, but an older brother to me and all my colleagues. He is one of the most encouraging and understanding people I've known.

I thank Mahmoud Abdelgalil (UCI Ph.D. candidate) discussions on Mathieu functions.

I would like to thank Dr. Amir S. Rezaei, Ph.D. and Nabil Khalifa (UCI Ph.D. candidate) for their advice implementing the CFD simulations.

Finally, I would like to thank the USAID for funding this research.

VITA

Ahmed Ismail EL-Nadi

EDUCATION

Master of Science in Mechanical and Aerospace Engineering **2021**
University of California, Irvine *Irvine, California*

Bachelor of Science in Mechanical Engineering **2016**
Zagazig University *Zagazig, Egypt*

RESEARCH EXPERIENCE

Graduate Research Assistant **2016–2019**
Zagazig University *Zagazig, Egypt*

TEACHING EXPERIENCE

Teaching Assistant **2016–2019**
Zagazig University *Zagazig, Egypt*

ABSTRACT OF THE THESIS

Theoretical Modeling of Unsteady Aerodynamic Loads on Plunging Airfoils in a Subsonic Compressible Flow

By

Ahmed Ismail EL-Nadi

Master of Science in Mechanical and Aerospace Engineering

University of California, Irvine, 2021

Professor Haithem E.Taha, Chair

The aerodynamic loads on a plunging flat plate are computed using Mathieu functions for different subsonic compressible Mach numbers and large range of reduced frequency (0-15). The obtained theoretical results are validated against previous theoretical results and simulations of the unsteady inviscid flow. The theoretical aerodynamic loads showed a good agreement to the CFD simulations. Results indicate that for small frequencies, the compressibility effect on the compressible aerodynamic loads is imperceptible. For high oscillation frequencies, the total lift phase approaches zero, in contrast to the behavior of the incompressible fluids. For a constant free stream velocity, the number of the dipole sources, distributed along the plate surface, increases as the reduced frequency K increases.

The compressible circulatory and non-circulatory frequency response functions are presented. The high frequency gain K_{hf} of the circulatory lift frequency response function decreases as the Mach number increases. The non-circulatory lift transfer function magnitude decreases as Mach number increases. Fluid compressibility induces a phase lag between the non-circulatory lift and the fluid motion. Finally, the reduced frequency has an insignificant effect on the non-circulatory transfer function phase lag at high K values.

Chapter 1

Introduction and Literature Review

1.1 Introduction and Research Motivation

Modern aviation history goes back to over a century ago when wright brothers successfully flew the kite "Flyer" for 12 seconds. Since these early attempts, aviation becames essential for industry, transportation, military activities and space exploration. Research continued to deeply understand aviation limitations to manufacture faster, larger and lower cost airplanes.

Determination of lift and moment of a lifting surface in steady, incompressible and inviscid flow has been a topic of interest since the early years of the twentieth century for its simplicity. The desire to eliminate the dangerous effects of flutter and dynamic stall motivated the researchers to account for unsteadiness, for deep understanding of such unsteady phenomena. Although the results of the incompressible aerodynamic theories played an important role in aviation development, the need for higher speed and reliable aircraft formed a challenge for researchers as compressibility and viscosity effects should be considered.

The compressibility extension of the unsteady, incompressible, theories is involved and can't

be achieved by the application of Prandtl-Glauert transformation. To account for compressibility, the boundary value problem governing the fluid motion should be transformed for this purpose. In addition to the compressibility effect that has been accounted for by researchers in the first half of twentieth century, the effect of viscosity on unsteady aerodynamics was attacked recently for incompressible fluids.

As illustrated in the introduction, the motivation for the present research is to examine the compressibility effect on lifting surfaces aerodynamic loads and to grasp the impact of high oscillation frequencies on unsteady aerodynamics. The aim of this work isn't to develop a new unsteady aerodynamic theory. Rather we examine the accuracy of existing theories and investigate the effect of compressibility.

1.2 Literature Review

The theories presented in this thesis encounters a combination of free stream flow variables and small disturbance variables. In order to eliminate confusion, the total variables are labeled with subscript "t", the free stream (far-field) variables are labeled with a subscript "o" while the remaining variables correspond to the flow disturbance. The equations presented in the following two sections corresponds to the total variables without linearization assumptions.

1.2.1 Basic Aerodynamic Concepts

Fluid mechanics basic concepts that are heavily used in this thesis are outlined in this section. Governing equations and potential flow vorticity will be reviewed.

Continuity and Momentum Equations

In the present work, compressible subsonic flow is considered with Mach number ranging from 0.35 to 0.6 with high density variation. The general continuity equation can be written as [1]

$$\frac{\partial \rho_t}{\partial t} + \nabla \cdot (\rho_t \boldsymbol{V}_t) = 0 \tag{1.1}$$

The equation of motion for a fluid element moving in a compressible Newtonian fluid is referred to as momentum equation or Navier-Stokes equation and can be expressed as [1]

$$\rho_t \frac{D\boldsymbol{V}_t}{Dt} = \rho_t \boldsymbol{g} - \nabla P_o + \mu^* \nabla^2 \boldsymbol{V}_t \tag{1.2}$$

Neglecting body forces and assuming inviscid fluid ($\nu = 0$), the equation is reduced to the Euler equation of the form

$$\rho_t \left(\frac{\partial \boldsymbol{V}_t}{\partial t} + \boldsymbol{V}_t \cdot \nabla \boldsymbol{V}_t \right) = -\nabla P_t. \tag{1.3}$$

Vorticity Transport in Compressible Flow

Vorticity is a core feature of fluid dynamics. It's a measure of fluid rotationality and defined as $\boldsymbol{\Omega} = \nabla \times \boldsymbol{V}_t$. The majority of fluid flows are vortical except for the simple potential flow assumption (sometimes referred to as vortex free flow). The vorticity transport equation for compressible flow is obtained by taking the curl of Navier-Stokes equation. For compressible fluid the transport equation can be expressed in the form

$$\frac{D\boldsymbol{\Omega}}{Dt} = -\boldsymbol{\Omega}\, \nabla \cdot \boldsymbol{V}_t + (\boldsymbol{\Omega} \cdot \nabla)\mathbf{V}_t - \frac{\nabla P_t \times \nabla \rho_t}{\rho_t^2} + \nabla \times \left(\frac{\nabla \cdot \boldsymbol{\tau}}{\rho_t} \right) \tag{1.4}$$

The first term describes the vortex stretching due to compressibility effects while the second term on the right hand side corresponds to vortex stretching or tilting because of velocity gradient. For a non-barotropic fluid, the third term, the pressure and density gradients, can be considered as a source of vorticity. The last term describes the vorticity diffusion and the spread of vorticity away from its source while moving with the flow. Flow over a solid surface, curved shock waves and Coriolis forces are major sources of vorticity. Blandford [2] discussed in details vorticity characteristics and its sources.

Potential Flow

Potential flow is an inviscid ($\mu^* = 0$) and irrotational ($\boldsymbol{\Omega} = 0$) flow. In potential flow the velocity field can be expressed as the gradient of a scalar function ϕ_t usually called potential function in the form $\boldsymbol{V}_t = \nabla\phi_t$. In Cartesian coordinates, the velocity components can be expressed as

$$u_t = \frac{\partial\phi_t}{\partial x}, \qquad v_t = \frac{\partial\phi_t}{\partial y}, \qquad w_t = \frac{\partial\phi_t}{\partial z}. \tag{1.5}$$

1.2.2 Kutta–Joukowski Lift Theorem

The definition of circulation played a crucial role in the development of aerodynamics lift theory. Circulation is defined as the line integral of the flow velocity vector around a closed curve [3]. The curve can move with the fluid and its shape can change with time. Circulation is expressed in terms of the velocity vector as

$$\Gamma = \oint \boldsymbol{V}_t \cdot d\boldsymbol{l} \tag{1.6}$$

where d$\boldsymbol{l}$ is the line segment. It can be alternatively defined as the surface integral of vorticity over the surface boundary by a closed curve; it's a measure of vortex strength.

The kutta-Joukowski lift theorem relates the circulation around the airfoil to the lift generation. In potential flow, the lift is generated by superposition of free stream, doublet and vortex. Using conformal mapping, the lift per unit span can be expressed as

$$L = -\rho_o U \Gamma \tag{1.7}$$

The flow is irrotational every where except at the origin as the vortex center exist. Anderson [3] showed that the circulation around any closed curve in the flow field excluding the airfoil origin vanishes. Also, from kelvin circulation theorem, the circulation total derivative (material derivative) for the same fluid elements is zero assuming neglected body forces.

A physical meaning can be given to circulation by observing the flow around an airfoil. A stationary airfoil in a stagnant fluid will have zero circulation everywhere including a curve surrounding the airfoil surface as shown in figure 1.1a. As illustrated in figure 1.1b, immediately after starting the flow around the airfoil at $t = 0^+$, the flow will curl around the trailing edge from the lower surface to the upper surface with high velocity creating a point vortex. Later in time, the created vortex at the trailing edge will convect downstream (assuming no flow separation) and usually named as the starting vortex. The curve will stretch downstream to include the starting vortex and the airfoil surface. The total circulation on the curve should remain zero as we follow the same fluid elements. A circulation with a strength equal to the starting vortex strength but opposite sign should present and usually referred to as bound circulation $\Gamma_b = -\Gamma_{st}$, where Γ_{st} is the starting vortex strength. Figure 1.1c shows the steady state flow around the airfoil including the bound circulation and the starting vortex.

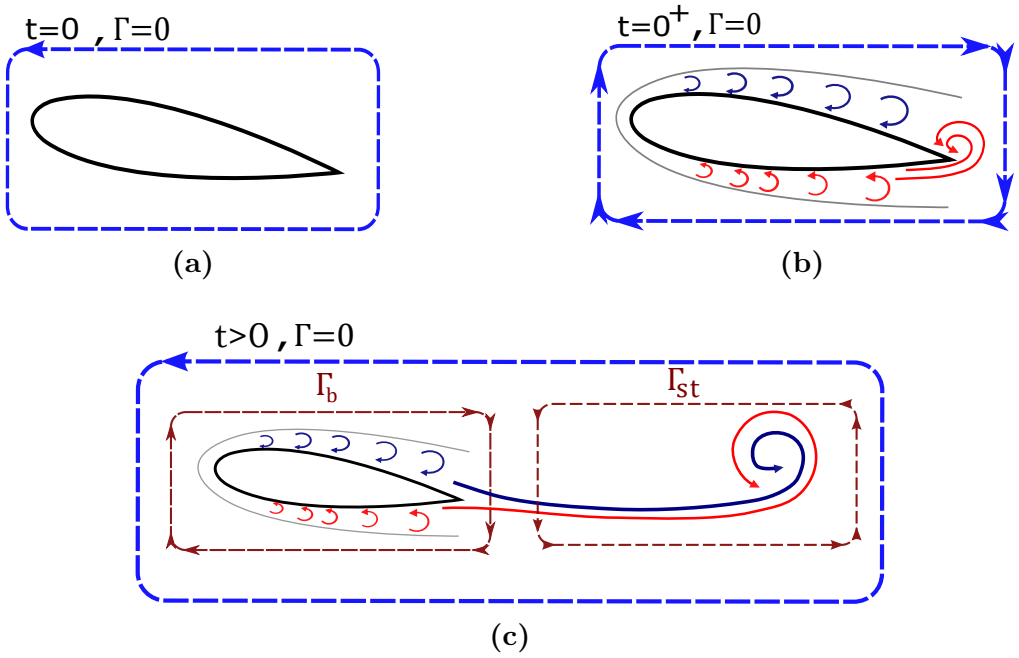

Figure 1.1: (a)A closed contour around the airfoil in a stagnant fluid resulting in a zero total circulation. (b) Immediately after starting the flow, the flow will curl around the sharp trailing edge from the lower surface to the upper surface. (c) The starting vortex is convected downstream with a strength Γ_{st} balancing a bound circulation around the airfoil Γ_b to satisfy the zero total circulation condition.

1.2.3 Steady, Incompressible Thin Airfoil Theory

The steady thin airfoil theory was developed by Munk and Glauert [3]. For high speed flows, viscosity effect is confined to a thin layer around the airfoil surface, so its effect is negligible in most steady and unsteady airfoil theories. The camber line is replaced by a sheet of vortices [3] usually called bound vortex $\gamma_b(x)$ as shown in figure 1.2a and 1.2b. The strength distribution of the bound vortex $\gamma_b(x)$ can be determined by satisfying the no-penetration boundary condition on the airfoil surface and Kutta-condition at the trailing edge. As shown in figure 1.2c, the kutta-condition ensures that the flow leaves smoothly of the trailing edge using $\gamma_{TE} = 0$.

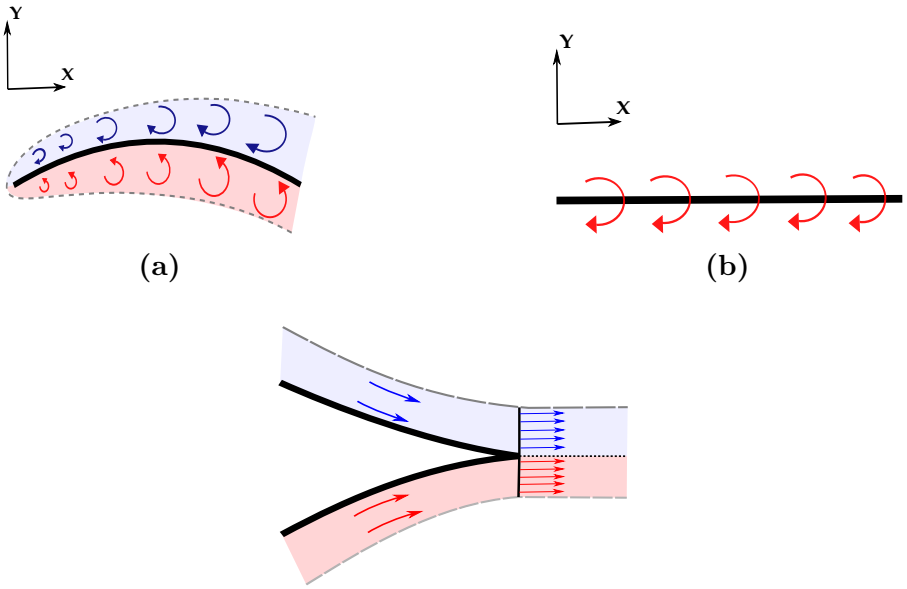

Figure 1.2: (a) Boundary layer around a flat plate showing the vorticity directions on the upper and lower surfaces. (b) Vortex sheet representing flow over a flat plate. The vorticity is rotating in a clockwise direction resulting in high flow speed on the upper surface and low speed on the lower surface of the plate. (c) Flow leaving smoothly of the trailing edge (Kutta-condition), assuming vanishing vortex strength at the trailing edge $\gamma_{TE} = 0$.

For symmetric airfoil with no camber, the bound vortex can be expressed as [3]

$$\gamma_b(\theta) = 2\alpha U \frac{(1+\cos\theta)}{\sin\theta}, \qquad at \qquad x = 0 \rightarrow \theta = 0, \quad x = 2b \rightarrow \theta = \pi \tag{1.8}$$

The total lift per unit span is

$$L = 2\pi\rho_o b U^2 \alpha. \tag{1.9}$$

Kutta-Joukowski theorem is used in the development of Eqn. (1.9) in the case of steady flow without separation.

1.2.4 Unsteady Thin Airfoil Theory

As mentioned in section (1.2.2), the steady lift is generated due to the bound circulation. The bound circulation is formed later in time, after impulsively starting the flow, and the starting vortex is shed away behind the airfoil. In the unsteady airfoil theory, the vortex sheet over the airfoil (bound vortex) will be a function of position and time $\gamma_b(x,t)$ and the wake vorticity effect on the down-wash will be considered.

The unsteady, inviscid, airfoil theories are complicated, so linearization of the governing equations and boundary conditions is applied for further simplification. Lin [4] and Miles [5] summarized the conditions for linearization and explicitly mentioned the conditions required for small disturbance theory to be applied. The velocity and pressure disturbances should be small compared to the free stream conditions. For these assumptions to be applied, the following conditions should be met

$$\frac{\delta}{c} << 1, \qquad K\delta << 1, \qquad M\delta << 1 \quad and \qquad KM\delta << 1, \tag{1.10}$$

where δ is the airfoil motion amplitude. If the first two conditions of Eqn.(1.10) are violated, the vertical velocity over the airfoil surface will be large and the small perturbation assumption isn't fulfilled [6]. If the remaining conditionds of Eqn. (1.10) are not satisfied, the flow will be hyper-sonic and the pressure disturbance by the airfoil will be large [7].

Incompressible Thin Airfoil Models

The unsteady thin airfoil theories were first developed for incompressible fluids by Theodorsen [8]. He developed a model of an airfoil performing oscillatory motion in an inviscid incompressible fluid. Gulcat [9] discussed the effect of simple harmonic motion of the form $Z(x,t) = \overline{H}e^{i\omega t}$.

The total lift coefficient amplitude is expressed as [9]

$$\overline{C_L}(K) = -2C(K)\int_{-1}^{1}\sqrt{\frac{1+\xi}{1-\xi}}\,\frac{\overline{W''}(\xi)d\xi}{U} - 2iK\int_{-1}^{1}\sqrt{1-\xi^2}\,\frac{\overline{W''}(\xi)d\xi}{U} \tag{1.11}$$

The second term on the right hand side of Eqn. (1.11) represents the inertia forces related to the airfoil motion and known as apparent or added mass. Since this term is present even in quiescent medium, it's not affected by circulation and can be called non-circulatory lift. It's important to mention that some recent developments showed that non-circulatory lift encounters some circulatory contributions [10]. Circulatory and non-circulatory lift components will be discussed in more details in chapter 5. The first term in (1.11) is affected by the circulation build up over the airfoil and called circulatory lift. Theodorsen [8] function, $C(k)$, measures the lag between the lift generation and the airfoil motion and have the form

$$C(K) = \frac{H_1^{(2)}(K)}{H_1^{(2)}(K) + iH_0^{(2)}(K)} = F(K) + iG(K) \tag{1.12}$$

Figure 1.3 shows the plot of Theodorsen [8] function amplitude and phase, respectively. The function dc gain or quasi-steady gain is unity ($K_{dc} = 1$). The other end of the graph representing the high frequency gain, K_{hf}, is 0.5. From Theodorsen function, we can infer that for high frequencies the aerodynamic lift is half its corresponding steady-state value.

Compressible Thin Airfoil Models

For an airfoil traveling at speeds close to the speed of sound, compressibility effects can't be neglected. In opposite to the incompressible flow, the small pressure disturbance caused by the airfoil motion travels at a finite velocity equal to the speed of sound. For all the, compressible, unsteady theories the problem is transformed into an incompressible one by shrinking the lateral dimensions by the factor $\beta = \sqrt{1-M^2}$ and increasing the oscillation frequency by a factor $(1-M^2)^{-1}$ [11]. The presence of the first and second order time

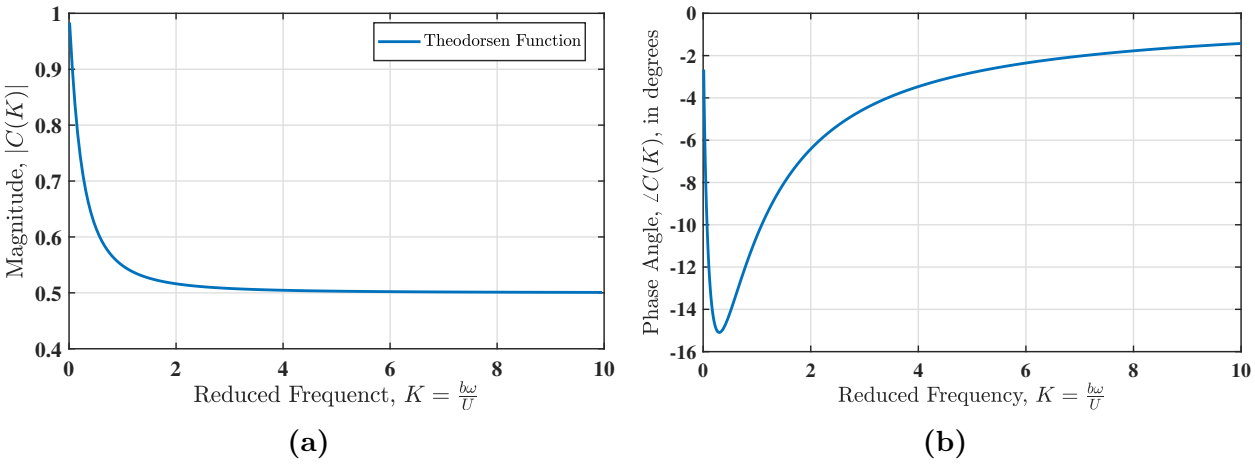

Figure 1.3: (a) Circulatory lift coefficient (Theodorsen [8] function magnitude). (b) Circulatory lift phase.

derivatives in the governing wave equation induces additional phase shift [12]. Sommerfeld radiation condition is applied to the compressible flow problem ensuring that the waves are traveling to infinity from the wing surface [13].

Analytical Models

The aerodynamic coefficients of pitching and plunging airfoils in subsonic compressible flow were first calculated and tabulated by Possio [14] for certain Mach numbers. He linearized the equations of motion for compressible flow and expressed the flow field in terms of acceleration potential. A solution of the governing wave equation is obtained in the form of doublet distributions over the airfoil chord. The resulting integral equation, relating the downwash and pressure distribution over the airfoil chord (doublet intensity), is known as Possio's integral equation. The integral equation is complicated and a closed-form analytical solution hasn't been obtained yet. As an approximate solution, Possio expressed the doublet intensity

in a series form that had been corrected by Frazer [15] and have the form

$$\Pi(x^*) = A_o^{'}\sqrt{\frac{1-x^*}{1+x^*}} + \sqrt{1-x^{*2}}\ \sum_{1}^{m} A_m^{'} x^{*m-1} \tag{1.13}$$

The coefficients are obtained by satisfying the no-penetration boundary condition at specific locations over the airfoil chord. Possio solved for three coefficients $A_o^{'}, A_1^{'}, A_2^{'}$. His solutions was based on three locations; leading edge, trailing edge and mid-chord point. Frazer repeated possio computations with higher numerical accuracy. He proposed an alternative series solution for the doublet intensity distribution using a trigonometric series in the form

$$\Pi(x) = A_o \cot\left(\frac{\theta}{2}\right) + \sum_{1}^{\infty} A_n \sin n\theta \tag{1.14}$$

The advantage of the alternative form is that the lift and moment can be computed exactly using the first three terms of the series, in opposite to Possio's series which requires the computation of all the terms. Efforts by Schade [16] and Dietze [17] continued to obtain a more accurate numerical solution for Possio's integral equation. Schade replaced the integral equation by a set of algebraic equations with legendre function expansion and and Dietze solved the equation iteratively.

A general three dimensional integral equation relating the downwash to the doublet intensity was derived by Kussner [18] and have the form

$$\begin{aligned}\Phi(x,y,z,t) =& \frac{1}{4\pi}\int\int_{F1}\int_{-\infty}^{x^{'}=x-\chi} dx^{'}d\chi d\eta \left(\sin\sigma(\eta)\frac{\partial}{\partial y} + \cos\sigma(\eta)\frac{\partial}{\partial z}\right) \\ & \frac{\Pi\left(\chi,\eta,t+\frac{x^{'}-x+\chi}{U}+\frac{x^{'}\beta}{c(1-\beta^2)}-\frac{\sqrt{x^{'2}+(1-\beta^2)[(y-y(\eta))^2+(z-z(\eta))^2]}}{c(1-\beta^2)}\right)}{\sqrt{x^{'2}+(1-\beta^2)[(y-y(\eta))^2+(z-z(\eta))^2]}}\end{aligned} \tag{1.15}$$

where the coordinate χ is parallel to the x-axis and forms a coordinate system with the coordinate η for a randomly located doublet on the airfoil surface. In his derivation of Eqn.(1.15), Kussner assumed a spherical wave solution for the linearized governing equation

and utilized the acceleration potential approach introduced by Prandtl [19]. Equation (1.15) was simplified to Prandtl's and Possio's integral equations.

A Convenient form of Possio's integral equation of infinite span can be obtained by integrating Eqn. (1.15) over τ from $-\infty$ to ∞ and defining Π as a sinusoidally pulsating doublet. The resulting equation will have the form[18][20]

$$\frac{\partial \Phi}{\partial n} = W''(x,0,t) = \frac{\sqrt{1-\beta^2}}{2\pi} \int_{-b}^{b} \Pi(\chi,t)\, e^{\frac{i\omega(\chi-x)}{U}} R\left(\beta, \frac{\omega(x-\chi)}{U(1-\eta^2)}\right) \frac{d\chi}{x-\chi}$$
$$where \tag{1.16}$$
$$R(\beta,y) = \frac{i\pi}{2}\beta y \int_{-\infty}^{y} e^{iu} H_1^{(2)}(\beta,u) \frac{du}{|u|}$$

Approximate solution of Eqn. (1.16) for small compressible Mach number is obtained by Miles [20] by expanding the kernel function, R, and Π in powers of Mach number. Later, Miles [12] extended his approximation to account for wide range of Mach numbers by expanding the kernel function in powers of y to first order in frequency.

For an oscillating wing of finite span with a harmonically pulsating doublet Eqn.(1.15) will be simplified to the form [21]

$$\overline{W''}(x,y) = \frac{1}{4\pi} \iint L(\chi,\eta)\, R(x_o,y_o)\, d\chi d\eta$$
$$where \tag{1.17}$$
$$R(x_o,y_o) = \lim_{z\to 0} \frac{\partial^2}{\partial z^2} e^{-\frac{i\omega x_o}{U}} \int_{-\infty}^{x_o} \frac{e^{i\overline{\omega}\left(\lambda - M\sqrt{\lambda^2+\beta^2 y_o^2+\beta^2 z^2}\right)}}{\sqrt{\lambda^2+\beta^2 y_o^2+\beta^2 z^2}}$$

where $\overline{\omega} = \frac{\omega}{U\beta^2}$, $x_o = x - \chi$ and $y_o = y - \eta$. Watkins [21] simplified the kernel function of Eqn.(1.17) to a form that can be evaluated and tabulated. The kernel function integral is separated into two parts that can be solved analytically. In his discussion regarding the function singularities, he showed that the integral is not only singular at $x_o = 0, y_o = 0$ but for the wake of the doublet ($x_o > 0$). He separated his general solution into singular and

non-singular parts and obtained formulas for some special cases ($M = 0, 1$).

An alternative solution using Green functions was introduced by W.Jones [11] to develop an integral equation relating the downwash distribution to the pressure field over the wing surface. He obtained the flutter derivatives of finite span wings. Jones didn't solve the, indeed, complicated compressible flow problem. Instead, he employed Prandtl–Glauert transformation to solve a simpler incompressible flow problem. The integral equation of the downwash distribution was divided into two parts as follows [11]

$$\begin{aligned} W'' + I_o =& \frac{1}{4\pi} \iint_{z\to 0} R \frac{\partial^2}{\partial z^2} \left(\frac{1}{r}\right) dxdy. \\ I_o =& \frac{1}{4\pi} \iint_{z\to 0} R \frac{\partial^2}{\partial z^2} \left(\frac{1 - e^{-ixr}}{r}\right) dxdy \end{aligned} \tag{1.18}$$

W.Jones solved Eqn. (1.18) using three different approximations. In two approximations, he assumed $I_o = 0$ where the flutter derivatives didn't show a good accuracy compared to the exact solution by Minhinnick [22]. The third approximation used I_o with accuracy up to first order in frequency. Figure 1.4 shows the total lift derivatives, L_z and $L_{\dot{z}}$ computed using the third approximation compared to Minhinnick at Mach number 0.7. The results showed a good agreement up to a reduced frequency $K = 0.4$. Later, W.Jones [23] extended the computations to account for higher frequency approximations and tabulated the flutter derivatives at different Mach numbers. The first order approximation is accurate at low frequency values. Increasing the frequency require increasing the order of approximation.

The wave equation governing the unsteady flow was, alternatively, solved by separating the perturbation, velocity or acceleration, potential into two parts both satisfying the wave equation. Timman [24], Timman and Van De Vooreen [25], Reissner [26], Haskind [27] and Billington [28] used the velocity potential method and obtained a solution in forms of Mathieu functions. A detailed explanation of Mathieu functions will be given in chapter 2.

The unsteady aerodynamic loads of low aspect ratio wings were calculated by Mazelsky [29].

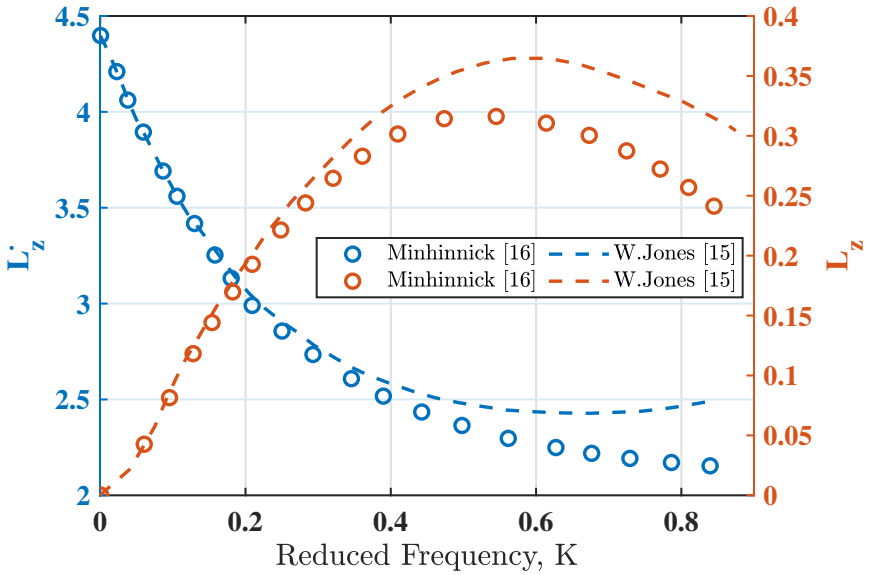

Figure 1.4: Total lift derivatives for $M = 0.7$.

The pitching and plunging motion of a rectangular and delta wings were investigated at several Mach numbers. The author simplified the equations by neglecting the flow derivatives in the stream wise direction and transformed the resulting wave equation into elliptic coordinates facilitating the use of separation of variables and Mathieu equations. Figure 1.5 shows the magnitude and phase of the lift coefficient due to plunging for a rectangular wing. From the figure it can be noticed that for $0 < K < 1$ the compressibility effect is small, however the compressibility have significant effect for high values of reduced frequency.

Similar to the velocity potential, the acceleration potential Φ is separated into two solutions $\Phi_1 + \Phi_2$. The reduced potential Φ_1 is usually referred to as "regular or non-circulatory" solution satisfying the normal acceleration on the airfoil. Results of aerodynamic loads for an oscillating airfoil in compressible flow had been given by Hofsommer [30], Kussner [31] and Timman and Van De Vooren [32]. Timman and Van De Vooren [32] obtained the lift and moment coefficients of pitching and plunging airfoil for five Mach number values. His computations of the regular solution was the same as mentioned before. The singular solution was approximated by a function satisfying the wave equation and the leading edge singularity. The results didn't agree to to Dietze [33] solution of possio's integral equation.

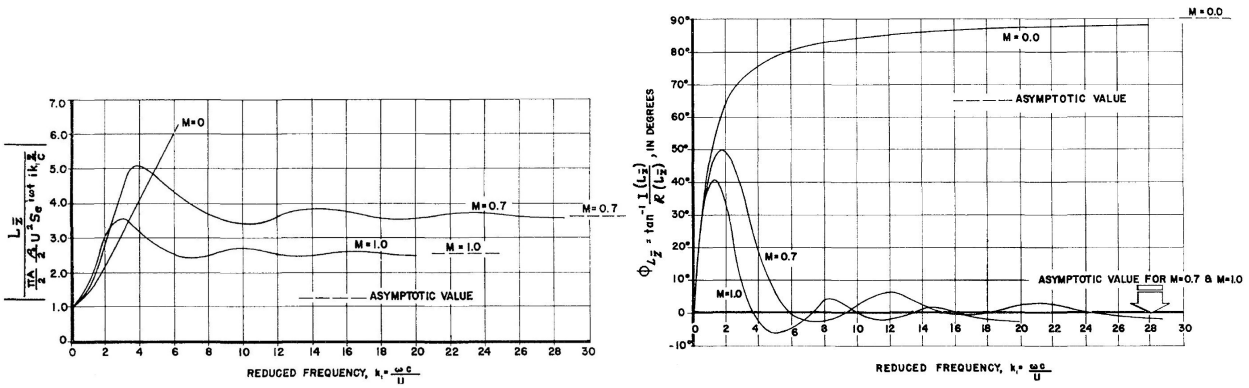

(a) **(b)**

Figure 1.5: (a) Total lift coefficient amplitude due to plunging of a rectangular wing [29]. (b) Total lift phase angle due to plunging [29].

R.Timman [34] extended the solution to satisfy the reciprocity relation after the concerns raised by Fettis [35].

In the context of the linearized theory and the corresponding assumption of negligible viscous effects, there exist a discrepancy between the measured aerodynamic loads and the theoretical counterpart. For a more accurate theoretical solution, Schwarz [36] and W. Jones [37] proposed a method usually referred to as "semi-empirical method". This method features the usage of the experimentally measured pressure distribution and the skeleton theory for estimating the change of the skeleton line (chord) at every instance. The semi-empirical method was originally applied to incompressible flow. However, with appropriate transformation, the compressible flow solution can be estimated.

Computational Models

In the vicinity of small perturbation theory, Cole [38] introduced a mixed finite difference scheme for transonic flow past a steady airfoil. Later, implicit scheme was developed by Ballhaus [39] to solve the two dimensional unsteady transonic flow past a moving airfoil. Su [40] introduced a time marching integral equation method for unsteady transonic flow

around airfoils. His method has the advantage of capturing a moving shock wave, by considering the non-linear terms, and faster convergence. Alternatively, a point iterative finite

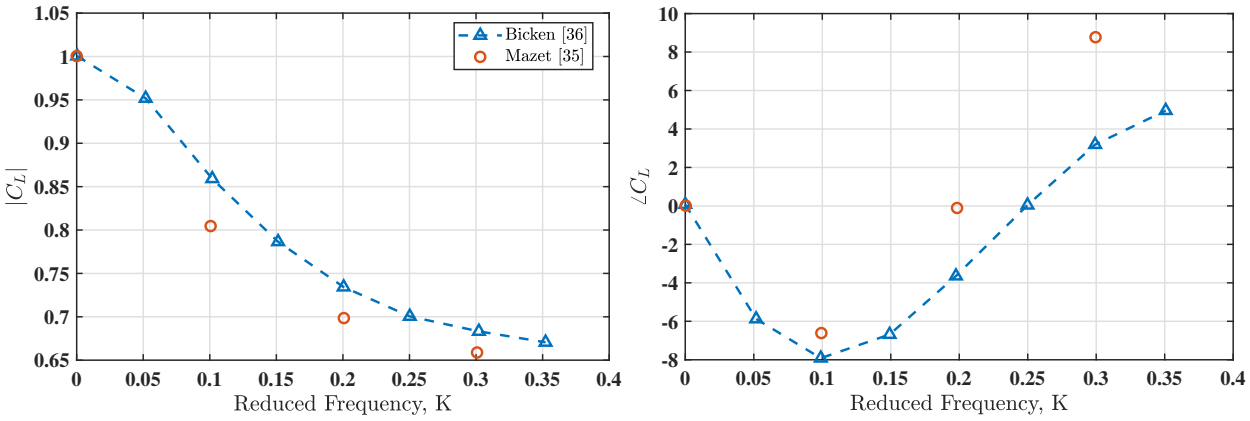

(a) **(b)**

Figure 1.6: Analytical results by Mazet [41] " ∘ " and Numerical by Bicken[42] " $-\triangle-$ " (a)Lift coefficient due for pitching. (b) Phase angle.

difference method was given by Bicken [42]. he obtained results for a harmonically pitching and plunging airfoil in subsonic and supersonic flows. As shown in figure 1.6, his method showed a good agreement to the analytical results by Mazet [41] for pitching airfoil in a subsonic compressible flow up to reduced frequency $K = 0.2$ at $M = 0.5$. The lift coefficient magnitude is comparable to the analytical results, in opposite to the phase angle, where the phase difference between both solutions increases as frequency increase.

1.3 Approach and Objective

It is declared that for oscillating airfoil in compressible flows there are a number of variables including compressibility, Mach number, airfoil shape, wing aspect ratio, oscillation frequency and viscosity which impact the aerodynamic loads and the flow field. The present thesis is directed towards comprehensive understanding of selected variables. The effort will aim to answer the following unanswered questions

1. What is the impact of fluid compressibility and oscillation frequency on the aerodynamic loads and phase lag?

2. What is the effect of the free stream Mach number on the total lift?

3. What is the effect of both the Mach number and oscillation frequency on the radiated pressure waves?

4. What is the impact of compressibility on both the circulatory and non-circulatory transfer functions?

In this thesis, the unsteady, compressible, aerodynamic theories given by Reissner and Haskind will be revisited and evaluated numerically to assess their accuracy and validity at high oscillation frequencies. In chapter 2, we review the Mathieu functions fundamentals. The purpose of this review is to validate our MATLAB code and investigate the accuracy of the function numerical computations. In chapter 3, a summary of Haskind's and Reissner's theories is provided with correction to minor mistakes in their derivations and analytical evaluation of some complicated integrals. The CFD simulations set-up and mesh motion characteristics are provided in chapter 4. Geometry and mesh parameters are discussed with their effect on solution accuracy. Finally, the aerodynamic loads at different Mach numbers, $M = 0.35, 0.5$ and 0.6, are presented in chapter 5. The circulatory and non-circulatory frequency response functions are also provided for plunging flat plate.

Chapter 2

Mathieu Functions Computation

As Mathieu functions are essential in the method used by Haskind [27] and Reissner [26] for the computations of aerodynamic loads. Mathieu functions definition and their numerical calculation methodology will be presented in this chapter. The code will be validated against previous results. Numerical errors and algorithm accuracy will be investigated to increase confidence in the computed aerodynamic loads.

2.1 Introduction

Mathieu functions are associated with waves propagation and usually expressed in elliptic cylinder coordinates. Historical background of Mathieu functions and examples of their applications in various boundary value problems are provided in references [43, 44, 45, 46, 47]. Computation of Mathieu equations isn't straight forward many articles investigated the numerical computations of these functions [48, 49]. As software or library routines for computing Mathieu equations aren't widespread, we made a custom MATLAB Toolbox. MATLAB software was selected for it's accuracy and speed in matrices computations and

it's ability to extend the results from single-precision to double precision easily.

At this stage, it's important to mention that there are many symbols used for expressing Mathieu functions in literature, Gutierrez [50] summarized most of the commonly used notations. In the present thesis, we employ Bibby's [51] notations for Mathieu functions.

2.2 Mathieu Functions

Mathieu functions are expressed in the elliptic cylinder coordinates. The transformation between the two coordinate systems have the form

$$x = Q\cosh\xi\ \cos\zeta, \qquad y = Q\sinh\xi\ \sin\zeta, \qquad z = z. \tag{2.1}$$

Figure 2.1 shows both Cartesian and Elliptic coordinates. For the elliptic coordinates, ξ ranges from 0 on the plate surface to ∞ and ζ ranges from 0 at the plate leading edge to π at the trailing edge.

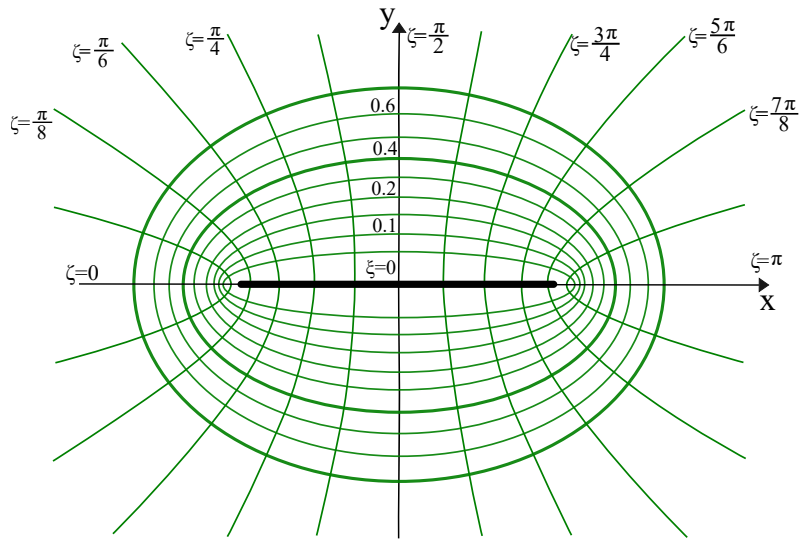

Figure 2.1: Cartesian(x, y) and elliptic (ξ, ζ) coordinates. ζ ranges from 0 at the plate leading edge to π at the trailing edge. ξ ranges from 0 on the plate surface to infinity at far field.

Mathieu equations are useful in solving the boundary value problems using separation of variables. Consider the Helmholtz equation of the form

$$\nabla^2\Psi + \kappa^2\Psi = 0. \tag{2.2}$$

Assuming a solution of the form $\Psi = \Psi_1(\xi)\ \Psi_2(\zeta)$. Substituting into Eqn.(2.2) and applying the transformation. The resulting functions can be expressed as

$$\frac{d^2\Psi_1}{d\xi^2} + (\Delta^2 - \kappa^2 Q^2\cos\xi^2)\Psi_1 = \frac{d^2\Psi_1}{d\xi^2} + (\Lambda - 2q\cos 2\xi)\Psi_1 = 0, \tag{2.3}$$

$$\frac{d^2\Psi_2}{d\zeta^2} - (\Delta^2 - \kappa^2 Q^2\cosh\zeta^2)\Psi_2 = \frac{d^2\Psi_2}{d\zeta^2} - (\Lambda - 2q\cosh 2\zeta)\Psi_2 = 0, \tag{2.4}$$

where Λ is a separation constant. Equation. (2.3) is known as "canonical Mathieu equation" and it's solution is usually called angular Mathieu functions. Equation. (2.5) is called "radial Mathieu equation" and it's solution is known as "radial Mathieu functions".

2.2.1 Angular Mathieu Functions

The angular Mathieu functions can be expressed as a series expansion in the form

$$ce_{2r+p}(\zeta, q) = \sum_{k=0}^{\infty} A_{2k+p}^{2r+p}\cos(2k+p)\zeta \quad where\ (r \geq 0;\ p = 0, 1), \tag{2.5}$$

$$se_{2r+p}(\zeta, q) = \sum_{k=0}^{\infty} B_{2k+p}^{2r+p}\sin(2k+p)\zeta \quad where\ (r \geq 0;\ p = 0, 1), \tag{2.6}$$

where r is the function order. The evaluation of the expansion coefficients, A, B, is necessary to define these functions. The expansion coefficients for each function satisfy a recurrence relation alongside with their normalization. For ce_{2r}, the recurrence relations can be expressed

as follows[51]

$$\begin{aligned} \lambda A_0^{2r} - qA_2^{2r} &= 0, \\ (\lambda - 4)A_2^{2r} - q(2A_0^{2r} + A_4^{2r}) &= 0, \\ \left(\lambda - (2k)^2\right) A_{2k}^{2r} - q(A_{2k-2}^{2r} + A_{2K+2}^{2r}) &= 0. \qquad (k \geq 2) \end{aligned} \tag{2.7}$$

The recurrence relations for the remaining three functions have similar formulas, reader is referred to Bibby [51] for further reading. The availability of powerful computing power allowed for the evaluation of the expansion coefficients through matrix routines [52, 53], unlike the continued fraction method that had been used before. Equation. (2.7) can be arranged in a matrix form as

$$\begin{bmatrix} 0 & \sqrt{2}q & 0 & 0 & & & & \\ \sqrt{2}q & 4 & q & 0 & & & & \\ 0 & q & 16 & q & & & & \\ & & & & \ddots & & & \\ & & & & q & (2k)^2 & q & \\ & & & & & & \ddots & \end{bmatrix} \begin{bmatrix} \sqrt{2}A_0^{2r} \\ A_2^{2r} \\ A_4^{2r} \\ \vdots \\ A_{2k}^{2r} \\ \vdots \end{bmatrix} = \lambda_{2k} \begin{bmatrix} \sqrt{2}A_0^{2r} \\ A_2^{2r} \\ A_4^{2r} \\ \vdots \\ A_{2k}^{2r} \\ \vdots \end{bmatrix} \tag{2.8}$$

From Eqn. (2.8), if any matrix dimension is N, then there exist N eigenvalues and corresponding N convectors for the expansion coefficients for each function order.

2.2.2 Radial Mathieu Functions

The two solutions of radial Mathieu functions are denoted as $Mc_i^{(j)}$ and $Ms_i^{(j)}$ where $j = 1, 2, 3$ and 4 represents the function kind and "i" the function order. Radial Mathieu functions have many forms [54]. A suitable form for numerical computations is the product of Bessel

functions as [51]

$$Mc_{2r}^{(j)}(\xi,q)=\frac{1}{\epsilon_s A_{2s}^{2r}}\sum_{k=0}^{\infty}(-1)^{k+r}A_{2k}^{2r}(q)\left[J_{k-s}(u_1)Z_{k+s}^{(j)}(u_2)+J_{k+s}(u_1)Z_{k-s}^{(j)}(u_2)\right], \quad (2.9)$$

$$Mc_{2r+1}^{(j)}(\xi,q)=\frac{1}{\epsilon_s A_{2s+1}^{2r+1}}\sum_{k=0}^{\infty}(-1)^{k+r}A_{2k+1}^{2r+1}(q)\left[J_{k-s}(u_1)Z_{k+s+1}^{(j)}(u_2)+J_{k+s+1}(u_1)Z_{k-s}^{(j)}(u_2)\right], \quad (2.10)$$

$$Ms_{2r}^{(j)}(\xi,q)=\frac{1}{B_{2s}^{2r}}\sum_{k=1}^{\infty}(-1)^{k+r}B_{2k}^{2r}(q)\left[J_{k-s}(u_1)Z_{k+s}^{(j)}(u_2)-J_{k+s}(u_1)Z_{k-s}^{(j)}(u_2)\right], \quad (2.11)$$

$$Ms_{2r+1}^{(j)}(\xi,q)=\frac{1}{B_{2s+1}^{2r+1}}\sum_{k=0}^{\infty}(-1)^{k+r}B_{2k+1}^{2r+1}(q)\left[J_{k-s}(u_1)Z_{k+s+1}^{(j)}(u_2)-J_{k+s+1}(u_1)Z_{k-s}^{(j)}(u_2)\right], \quad (2.12)$$

where $\epsilon_0=2$, $\epsilon_s=1$, for $s=1,2,3,....$, $u_1=\sqrt{q}e^{\xi}$, $u_2=\sqrt{q}e^{-\xi}$,$Z_p^1(u)=J_p(u)$, $Z_p^2(u)=Y_p(u)$, $Z_p^3(u)=H_p^{(1)}(u)$, $Z_p^4(u)=H_p^{(2)}(u)$ and A,B are the same expansion coefficients in Eqs.(2.5),(2.6).

The choice of the parameter "s" in Eqns.'(2.9)-(2.12) is arbitrary[47]. According to Van Buren [55], the choice of the parameter "s" can affect the convergence and accuracy of the summations. Many articles adopted different choices for this parameter [51]. The choice of $s=0$ or 1 was labeled by Bibby [51] as the "traditional approach". In our code we adobe the approach given by Bibby [51], Blanch [47] and Van Buren [55]. For this approach the value of "s" is chosen to be the position of the maximum absolute value in the selected eigenvector which correspond to the column number in the eigenvector matrix.

2.3 Code Validation

Before proceeding to investigate the calculation accuracy and various numerical errors, the code for Mathieu functions is validated against previous results given by Abramowitz [56].

Abramowitz results were calculated using the method of continued fraction. Figure. 2.2

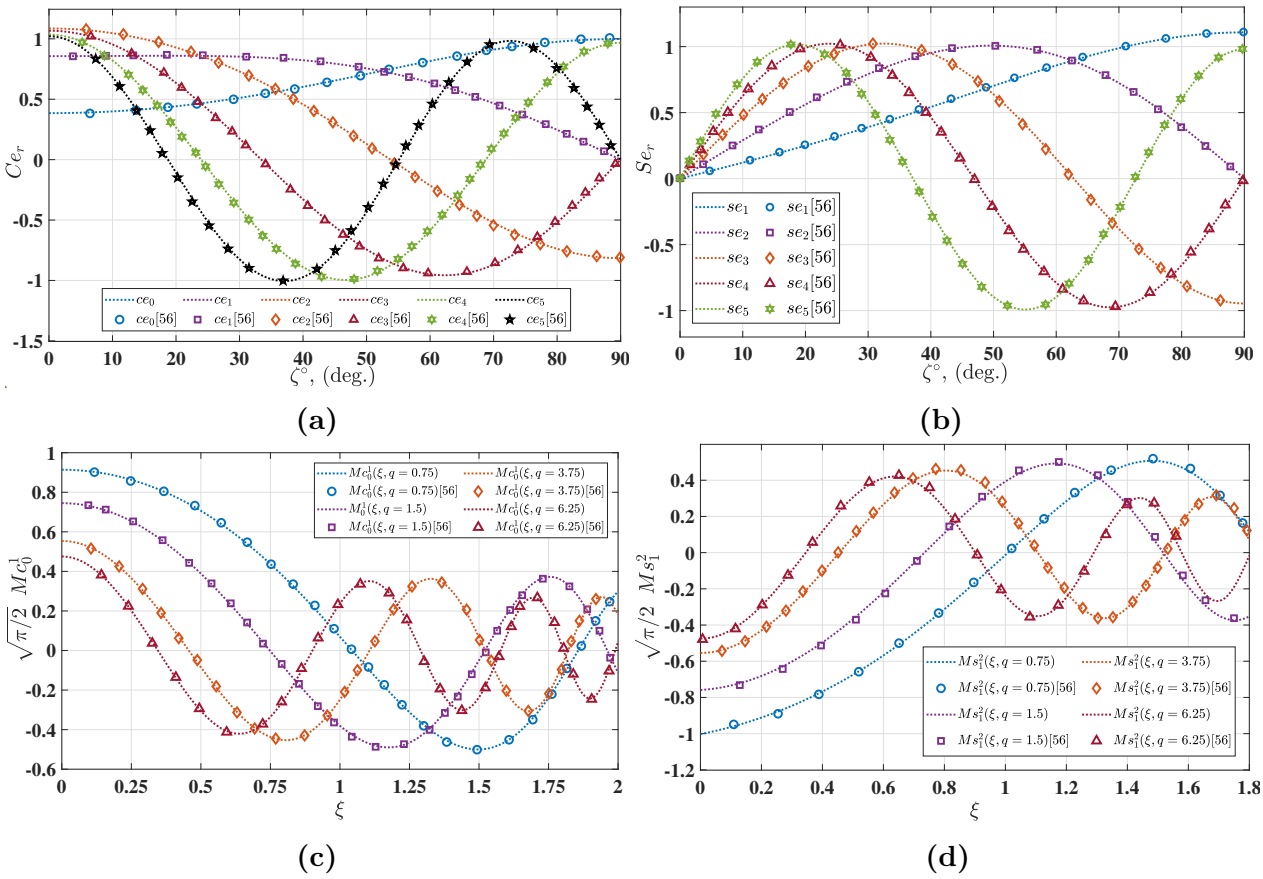

Figure 2.2: Even and Odd periodic Mathieu functions. (a) Even periodic Mathieu functions at ($q = 1$) compared to data given by Abramowitz [56]. (b) Odd periodic Mathieu functions at ($q = 1$) compared to data given by Abramowitz [56]. (c) Radial Mathieu function of the first kind for distinct q values and zero order compared to Abramowitz [56]. (d) Radial Mathieu function of the second kind for distinct q values and first order compared to Abramowitz [56].

shows the comparison between the MATLAB code and Abramowitz results. The angular and radial Mathieu functions,of different order, are plotted against the arguments ζ and ξ, respectively. Figures.(2.2a) and (2.2b) compares even and odd periodic Mathieu equations, respectively, for functions order (1 - 5) at $q = 1$. The radial Mathieu function of the first kind and zero order is shown in Fig. (2.2c) at four different values of q ranging from $q = 0.75$ to $q = 1.5$. In Fig. (2.2d) a calculation of radial Mathieu equations of the first order and second kind are presented at four values of q. For all q values, our calculations are in an excellent agreement with Abramowitz [56] and gives confidence to proceed with aerodynamic

loads computations.

2.4 Accuracy of Computations

As Mathieu functions have no closed-form analytical solution, the summation accuracy and numerical precision should be investigated [51]. From Eqns. (2.5)-(2.6), the angular Mathieu functions are function of the elliptic angle ζ, q and matrix size N. Van Buren [55] defined Subtraction error as a critical error source arising when adding two numbers of comparable magnitudes but opposite signs. Subtraction error have the form [51, 55]

$$Subtraction\ Error = \log_{10}\left|\frac{Sum_{+}}{Sum_{+} - Sum_{-}}\right|, \tag{2.13}$$

where Sum_{+} is the summation of all positive terms and Sum_{-} is the summation of the negative terms absolute value. As the parameter "q" has a significant effect on the subtraction error, it's important to investigate it's effect on the equations accuracy. Selected q values are shown in Table 2.1 at different M values.

Table 2.1: Parameter **"q"** for selected values of reduced frequency,K, and Mach number,M.

	M=0.35		M=0.5		M=0.6	
K	κ	q	κ	q	κ	q
0.1	0.0399	3.977×10^{-4}	0.0667	1.1111×10^{-3}	0.09375	2.1972×10^{-3}
5	1.9943	0.9943	3.3333	2.7778	4.6875	5.4932
10	3.9886	3.9772	6.6667	11.1111	9.375	21.9727
15	5.9829	8.9487	10.0	25	14.0625	49.438

Table. 2.1 shows the minimum and maximum values of "q" encountered in the aerodynamic loads computations and guides towards investigating Mathieu functions subtraction error in this range. In his article, Bibby [51] showed that the maximum subtraction error will always be associated with lowest function order. So, even and odd angular Mathieu function of zero and first order, respectively, will be investigated.

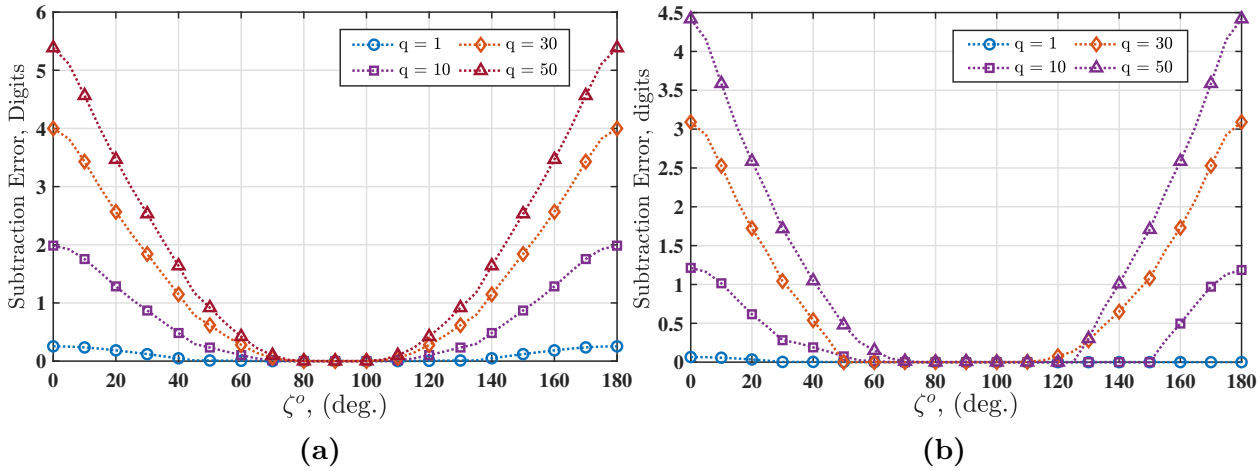

Figure 2.3: Subtraction error versus the elliptic angle ζ at $N = 100$. (a) Even angular Mathieu function of zero order $\boldsymbol{ce_0(\zeta, q)}$. The subtraction error increase as q increase and the maximum error is associated to angles 0 and π. (b) Odd angular Mathieu function of first order $\boldsymbol{se_1(\zeta, q)}$. The maximum subtraction error is associated to angles 0 and π.

Figure 2.3a shows the effect of the angle ζ on subtraction error for the angular Mathieu function of zero order $ce_o(\zeta, q)$. The maximum error of 5 digits is associated with angles $0, \pi$ at $q = 50$. Subtraction error of the odd Mathieu function of the first order is shown in Fig. 2.3b with maximum error at $0, \pi$ for $q = 50$. From the previous discussion it can be concluded that double-precision (15 decimal digits) computations is sufficient for accurate results.

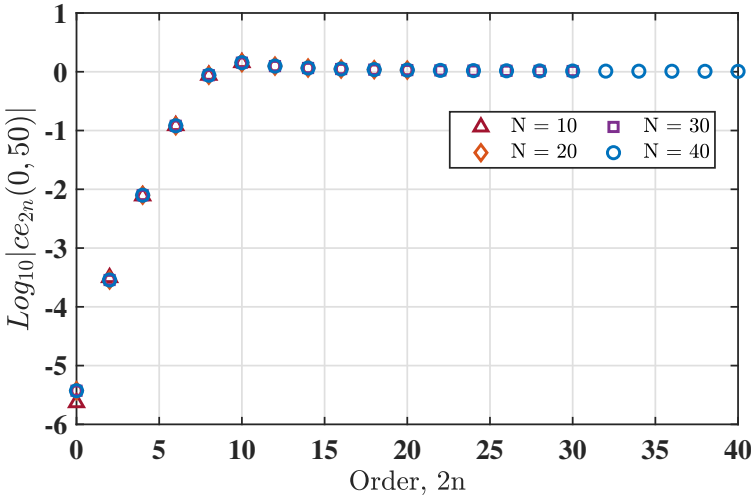

Figure 2.4: Plot of ce_{2n}, $n = 0, 1, ...$ for $\zeta = 0, q = 50$ at different values of matrix size,N.

Finally, the eigenvector matrix size effect on the solution accuracy is shown in figure 2.4. The figure shows the value of the function $Log_{10}|ce_{2n}(0, 50)|$ at different function orders using four eigenvector matrix sizes for comparison. The values of $q = 50$ is used as it corresponds to the highest values of subtraction error. As shown in Figure the function value is independent of the matrix size for $N = 20$ and higher. A matrix size of $N = 20$ will be used for the lift and moments calculations.

Chapter 3

Theoretical Modeling of Compressible Unsteady Aerodynamics

The problem of oscillating, two-dimensional, airfoil in subsonic flow using Mathieu functions had been solved by Reissner [26] and Haskind [27]. Both formulations are identical for non-circulatory lift. In the case of circulatory lift, each author used a different solution form for the governing equation. In this chapter, both derivations will be summarized with minor corrections. Analytical solution of the integral equations is also provided. As the notations used in both derivations are different, we employ Reissner's notations.

3.1 Equations of Motion and Boundary Conditions

A plane two-dimensional lifting surface with equation of the form $z = H(x,t)$ is placed in a uniform flow with a mean velocity component U in positive X-direction as shown in figure 3.1. The presence of the lifting surface caused the velocity field to disturb from U to $(U+u, w)$. The density will disturb from ρ_o to $(\rho_o+\rho)$ and the pressure from P_o to (P_o+p).

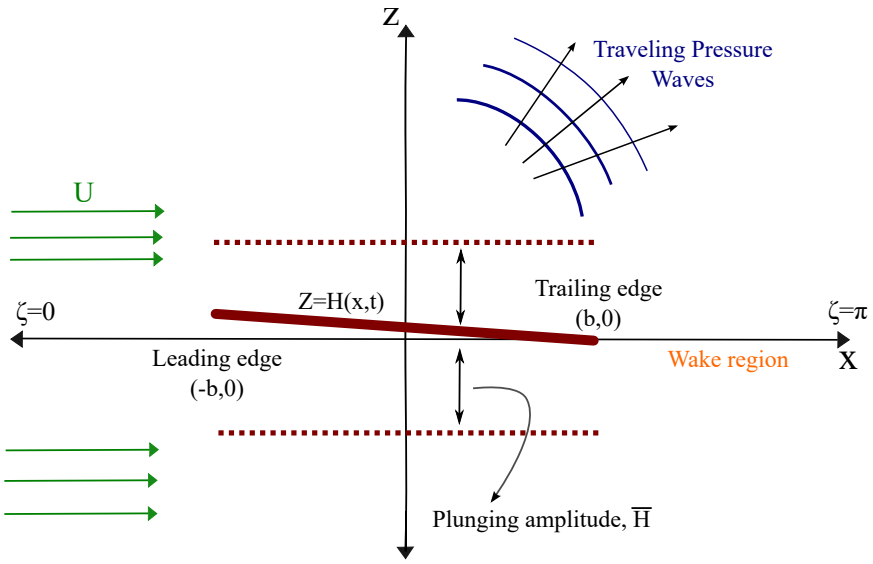

Figure 3.1: Diagram showing the plate orientation, free stream direction and the oscillatory plunging motion.

The linearized momentum and continuity equations will be expressed as

$$\frac{\partial u}{\partial t} + U\frac{\partial u}{\partial x} = -\frac{\partial}{\partial x}\left(\frac{p}{\rho_o}\right) \tag{3.1}$$

$$\frac{\partial w}{\partial t} + U\frac{\partial w}{\partial x} = -\frac{\partial}{\partial z}\left(\frac{p}{\rho_o}\right) \tag{3.2}$$

$$\frac{\partial \rho}{\partial t} + U\frac{\partial \rho}{\partial x} = -\rho_o\left(\frac{\partial u}{\partial x} + \frac{\partial w}{\partial z}\right) \tag{3.3}$$

Introducing the perturbation velocity potential ϕ, where $u = \frac{\partial \phi}{\partial x}$, $w = \frac{\partial \phi}{\partial z}$. Expressing the perturbation pressure in terms of the velocity potential by combining equations (3.1) and (3.2) in the form

$$p = -\rho_o\left(\frac{\partial \phi}{\partial t} + U\frac{\partial \phi}{\partial x}\right) \tag{3.4}$$

The governing convective wave equation is obtained by combining equations (3.4) and (3.3)

and is expressed as

$$\frac{\partial^2\phi}{\partial x^2}+\frac{\partial^2\phi}{\partial z^2}-\frac{1}{a^2}\left(\frac{\partial}{\partial t}+U\frac{\partial}{\partial x}\right)^2\phi=0, \tag{3.5}$$

The boundary conditions on the plane separating the upper and lower surfaces of the plate are as follows

$$|x|\leq b, \quad z=0, \quad \frac{\partial\phi}{\partial z}=\frac{\partial H}{\partial t}+U\frac{\partial H}{\partial x}, \tag{3.6}$$

$$x=b, \quad z=0, \quad \frac{\partial\phi}{\partial x} \quad finite, \tag{3.7}$$

$$x>b, \quad z=0, \quad \frac{\partial\phi}{\partial t}+U\frac{\partial\phi}{\partial x}=0, \tag{3.8}$$

$$x<b, \quad \phi=0. \tag{3.9}$$

Eq. (3.8) and (3.9) indicate a vortex sheet trails behind the plate. By considering the problem geometry and nature, a symmetry condition for the perturbation potential can be obtained as $\phi(x,-z,t)=-\phi(x,+z,t)$ which concludes that the perturbation potential is an odd function of z. Simplifying the governing equation and boundary conditions by introducing non-dimensional coordinate system of the form $X=\frac{x}{b}$ and $Z=\sqrt{1-M^2}\frac{z}{b}$.

Applying simple harmonic motion to the lifting surface by setting

$$\phi=e^{i(\omega t+\mu x)}\psi, \tag{3.10}$$

where $\mu=\frac{KM^2}{1-M^2}$. The variable $e^{i\mu x}$ and the constant μ are introduced to eliminate the first spatial derivative in equation (3.5). Substituting Eqn.(3.10) and the non-dimensional variables into Eqn. (3.5), then the governing equation will have the form

$$\frac{\partial^2\psi}{\partial X^2}+\frac{\partial^2\psi}{\partial Z^2}+\kappa^2\psi=0. \tag{3.11}$$

Equation. (3.11) and its corresponding boundary conditions is the famous exterior boundary value problem. Sommerfield radiation conditions is usually added to the exterior boundary value problems for uniqueness of the solution and have the form

$$\lim_{r\to\infty}\sqrt{r}\left[\frac{\partial\phi}{\partial r}+i\kappa\phi\right]=0, \qquad \lim_{r\to\infty}\left|\sqrt{r}\phi\right|<const. \tag{3.12}$$

Solution in the form of Mathieu equations will be appropriate by transforming the Cartesian coordinates (X, Z) into elliptic coordinates (ξ, ζ) as follows

$$X = Q\,\cosh\xi\,\cos\zeta, \quad Z = Q\,\sinh\xi\,\sin\zeta \tag{3.13}$$

where $0 \le \xi \le \infty$, $0 \le \zeta \le 2\pi$ and $Q = 1$.

The resulting differential equation (3.11) will have the form

$$\frac{\partial^2\psi}{\partial\xi^2}+\frac{\partial^2\psi}{\partial\zeta^2}+\kappa^2\left(\cosh^2\xi-\cos^2\zeta\right)\psi=0. \tag{3.14}$$

The function ψ can be separated as

$$\psi = \psi_1 + \psi_2 \tag{3.15}$$

where ψ_1 and ψ_2 are associated with the non-circulatory and the circulatory lift components, respectively. Using Eqn. (3.15), the boundary conditions in terms of elliptic coordinates will be expresses as

$$\xi = 0, \qquad \frac{1}{\sin\zeta}\frac{\partial\psi_1}{\partial\zeta} = g\left(\zeta\right), \qquad \frac{\partial\psi_2}{\partial\xi} = 0, \tag{3.16}$$

$$\xi = 0, \qquad \lim_{\xi\to 0}\left[\frac{1}{\sin\zeta}\left(\frac{\partial\psi_1}{\partial\xi}+\frac{\partial\psi_2}{\partial\xi}\right)\right]\ finite, \tag{3.17}$$

$$\zeta = 0, \pi, \qquad \psi_1 = 0, \qquad i\nu\psi_2+\frac{1}{\sinh\xi}\frac{\partial\psi_2}{\partial\xi}=0, \tag{3.18}$$

where

$$g(\zeta) = \frac{U e^{-i\mu\cos\zeta}}{\sqrt{1-M^2}} \left[ik\overline{H} + \frac{\partial \overline{H}}{\partial x} \right], \qquad \nu = \frac{K}{1-M^2} \tag{3.19}$$

The pressure amplitude over the airfoil surface have the form

$$\overline{p_a} = -\frac{\rho_o U}{b} e^{i\mu\cos\zeta} \left(i\nu\psi(0,\zeta) - \frac{1}{\sin\zeta} \frac{\partial\psi(0,\zeta)}{\partial\zeta} \right). \tag{3.20}$$

$$\tag{3.21}$$

3.2 Solution in The Form of Mathieu Functions

A solution of Eqn. (3.14) and its associated boundary conditions can be obtained by separation of variables as explained in chapter 2. Expressing ψ as the product of two functions $F(\xi)G(\zeta)$ and using (3.14), the resulting two equations will have the form

$$\frac{d^2G}{d\zeta^2} + \left[(\lambda^2 - 2q) - 2q\,\cos 2\zeta \right]\, G = 0, \tag{3.22}$$

$$\frac{d^2F}{d\xi^2} - \left[(\lambda^2 - 2q) - 2q\,\cosh 2\xi \right]\, F = 0, \tag{3.23}$$

where λ is a separation constant. The function G is Sturm-Liouville equation which is periodic with period 2π and its solution is the angular Mathieu functions. The solution of the function $F(\xi)$ is chosen to be the Radial (or modified) Mathieu functions of the forth kind, as its asymptotic expansion satisfies the wave (radiation) condition at infinity [50].

Haskind [27] and Reissner [26] used different normalization of the Mathieu functions expansion coefficients. In order to compare both solutions, the normalization is eliminated in the present thesis for both angular and radial Mathieu functions. Therefore, the equations to be mentioned in the subsequent two sections are reformulated from this perspective.

Form the above equations, the solution may be combined and described in a series form as follows

$$\psi = \sum_{m=0}^{\infty} a_m ce_m(\zeta) Mc_m^{(4)}(\xi) + \sum_{m=0}^{\infty} b_m se_m(\zeta) Ms_m^{(4)}(\xi), \tag{3.24}$$

where a_m and b_m are two constants to be determined by the application of boundary conditions and the plate motion.

3.3 Non-Circulatory Flow Component

The noncirculatory flow component indicated as ψ_1 can be expressed as

$$\psi_1 = \sum_{m=1}^{\infty} b_m se_m(\zeta) Ms_m^{(4)}(\xi). \tag{3.25}$$

Substituting boundary condition Eqn. (3.16) into Eqn. (3.25) and using orthogonality relations, the coefficient b_m will be

$$b_m = \frac{\int_0^{\pi} \sin\zeta \; g(\zeta) se_m(\zeta) \; d\zeta}{\int_0^{\pi} Ms_m^{'(4)}(0) \; [se_m(\zeta)]^2 d\zeta}^{*} \tag{3.26}$$

The pressure amplitude at the airfoil corresponding to the noncirculatory lift ${\overline{p}_a}^{(1)}$ can be obtained by substituting Eq. (3.20) into Eqn. (3.25) and will be in the form

$${\overline{p}_a}^{(1)} = -\frac{\rho_o U}{b} e^{i\mu\cos\zeta} \left[i\nu \sum_{m=1}^{\infty} b_m se_m(\zeta) Ms_m(0) - \frac{1}{\sin\zeta} \sum_{m=1}^{\infty} b_m se_m^{'}(\zeta) Ms_m(0) \right] \tag{3.27}$$

*This equation is a reformulation of Eq. (72) in [26] without normalization.

Integrating the pressure distribution (3.27) over the plate chord, the non-circulatory lift amplitude $\overline{L}^{(1)}$ is

$$\begin{aligned}\overline{L}^{(1)} &= 2b\int_0^{\pi} \overline{p}_a{}^{(1)} \sin\zeta \, d\zeta \\ &= -2\rho_o U \sum_{m=1}^{\infty} b_m M s_m(0) \int_0^{\pi} e^{i\mu\cos\zeta} \left[i\nu \sin\zeta \; se_m(\zeta) - se_m^{'}(\zeta) \right] d\zeta \; ^*\end{aligned} \tag{3.28}$$

The moment about the mid-chord point can be expressed as

$$\overline{M}^{(1)}(0) = -2\rho_o U b \sum_{m=0}^{\infty} b_m M s_m^{(4)}(0) \int_0^{\pi} \cos\zeta e^{i\mu\cos\zeta} [i\nu \sin\zeta \; se_m(\zeta) - se_m^{'}(\zeta)] \, d\zeta \tag{3.29}$$

Evaluating the coefficient b_m depends on the type of airfoil motion.

3.3.1 Plunging Motion

For an airfoil performing plunging motion of the form $\overline{H}(x) = \overline{h}$, Eqn. (3.26) can have a closed form expression using Eqn. (3.19) and expressed as

$$b_{m\bar{h}} = \frac{iUk\overline{h}I_m}{\sqrt{1-M^2}\; M s_m^{(4)'}(0) \int_0^{\pi} \left[se_m(\zeta) \right]^2 d\zeta} \tag{3.30}$$

where

$$I_m = \int_0^{\pi} e^{-i\mu\cos\zeta} \sin\zeta \; se_m(\zeta) \, d\zeta = \frac{\pi}{\mu} \sum_{n=1}^{\infty} B_{mn} \; n(-1)^n \; i^{n+1} J_n(\mu)^{\dagger} \tag{3.31}$$

---

*This equation corresponds to Eqn.(58) in [26]. The author performed the summation inside the integral over n and it should be over m. The summation over n is applied to the expansion coefficients of angular Mathieu equation in a following step.

†This integral calculation is a correction to Eq.(73) in [26]. Detailed derivation in the appendix A

3.3.2 Pitching motion

The pitching motion of an airfoil about its mid-chord point is

$$\overline{H}(x) = \overline{\alpha}\left(x + \frac{b}{iK}\right)^{*} \tag{3.32}$$

The coefficient $b_{m\overline{\alpha}}$ will be expressed as

$$b_{m\overline{\alpha}} = \frac{U\overline{\alpha}b\int_0^{\pi}(iK\cos\zeta + b\ + 1)e^{-i\mu\cos\zeta}se_m(\zeta)\ d\zeta}{\sqrt{1-M^2}Ms_m^{'(4)}(\zeta)\int_0^{\pi}[se_m(\zeta)]^2\ d\zeta} \tag{3.33}$$

Haskind [27] expressed the coefficient b_m in terms of the vertical velocity amplitude instead of the displacement amplitude. As Reissner [26] and Haskind formulation of the non-circulatory lift are identical, Reissner's formulation only is presented.

3.4 Circulatory Flow component

The function representing the circulatory component ψ_2 have the form

$$\psi_2 = \sum_{m=0}^{\infty} a_m ce_m(\zeta)Mc_m(\xi) \tag{3.34}$$

Introducing function $W(x,z)$, connected to the function ψ_2 as follows

$$\frac{\partial\psi_2}{\partial X} + i\nu\psi_2 = \frac{\partial W}{\partial Z} \tag{3.35}$$

*This equation is a correction to Reissner's [26] form, Eqn.(70). He ignored the free stream velocity component.

Satisfying the differential equation $\nabla^2 W + \kappa^2 W = 0$ and radiation condition at infinity. The boundary condition Eqn. (3.16) for ψ_2 and W can be expressed as

$$Z = 0, \quad |X| \leq 1, \quad \frac{\partial^2 W}{\partial X^2} + \kappa^2 W = 0 \tag{3.36}$$

Reissner [26] expressed the solution of Eqn. (3.36) as

$$Z = 0, \quad |X| \leq 1, \quad W(X,0) = A\cos\kappa X + B\frac{\sin\kappa X}{\kappa} \tag{3.37}$$

Two equations relating the coefficients A and B are required to solve the circulatory lift problem. The first of which can be obtained by applying the remaining boundary conditions for $W(X,Z)$ and integrating from $-\infty \to X$. The equation will have the form

$$\begin{aligned} &A\left[e^{-i\nu}(\kappa\sin\kappa - i\nu\cos\kappa) + (\kappa^2-\nu^2)\sum_{m=0}^{\infty}\alpha_m ce_m(\pi)\int_0^{\infty} e^{-i\nu\cosh\xi} Mc_m^{(4)}(\xi)\sinh\xi\right] \\ &+B\left[e^{-i\nu}(\cos\kappa + \frac{i\nu}{\kappa}\sin\kappa) + (\kappa^2-\nu^2)\sum_{m=0}^{\infty}\beta_m ce_m(\pi)\int_0^{\infty} e^{-i\nu\cosh\xi} Mc_m^{(4)}(\xi)\sinh\xi\right] \end{aligned} \tag{3.38}$$

*

where

$$\alpha_m = \frac{\int_0^{\pi}\cos\kappa\ \cos\zeta ce_m(\zeta)d\zeta}{\int_0^{\pi} Mc_m^{(4)}(0)[ce_m(\zeta)]^2 d\zeta}, \qquad \beta_m = \frac{\int_0^{\pi}\kappa^{-1}\sin\kappa\ \cos\zeta ce_m(\zeta)d\zeta}{\int_0^{\pi} Mc_m^{(4)}(0)[ce_m(\zeta)]^2 d\zeta} \tag{3.39}$$

The circulatory lift amplitude can be expressed as

$$\overline{L}^{(2)}|_{Reissner} = -2\rho_o U\left[A\sum_{m=1}^{\infty}\alpha_m\int_0^{\pi} e^{i\mu\cos\zeta} ce_m(\zeta)d\zeta + B\sum_{m=1}^{\infty}\beta_m\int_0^{\pi} e^{i\mu\cos\zeta} ce_m(\zeta)d\zeta\right] \tag{3.40}$$

*Analytical solution of the infinite integral can be found in Appendix B

The circulatory pitching moment, about mid-chord point, for plunging motion is

$$\begin{aligned}\overline{M}^{(2)}|_{Reissner} = -2\rho_o U b(A\sum_{m=1}^{\infty}\alpha_m\int_0^{\pi} e^{i\mu\cos\zeta}ce_m(\zeta)\ \cos\zeta d\zeta \\ +B\sum_{m=1}^{\infty}\beta_m\int_0^{\pi} e^{i\mu\cos\zeta}ce_m(\zeta)\ \cos\zeta d\zeta)\end{aligned} \tag{3.41}$$

On the other hand, Haskind [27] obtained an expression for $W(X,Z)$ in an integral form by excluding the sources on the airfoil chord

$$W(x,z) = \int_{-1}^{+1}\gamma(s)H_0^{(2)}(\kappa r)ds, \qquad r^2 = (X-s)^2 + Z^2 \tag{3.42}$$

where $\gamma(s)$ is expressed as summation of angular and radial Mathieu equations. Equation (3.42) satisfies boundary conditions and radiation principle at infinity. His solution of Eqn. (3.36) have the form

$$W(X,0) = Ae^{i\kappa X} + Be^{-i\kappa X}. \tag{3.43}$$

Using Eq. (3.42) and satisfying boundary conditions on the plane of symmetry and radiation principle at infinity, Haskind [27] obtained an alternative expression to Eq. (3.38) of the form

$$A\left(C_+ + \frac{i\ e^{i(\kappa-\nu)}}{\kappa-\nu}\right) + B\left(C_- - \frac{i\ e^{-i(\kappa+\nu)}}{\kappa+\nu}\right) = 0\ ^*$$

where

$$c_\pm = \frac{1}{2i}\sum_{m=0}^{\infty} Mc_m'^{(4)}(0)\ \alpha_\pm^{(m)}\int_0^{\pi} f(\cos\zeta)\ ce_m(\zeta)\ d\zeta, \qquad \alpha_\pm^{(m)} = \frac{\int_0^{\pi} e^{\pm i\kappa\cos\zeta}ce_m(\zeta)d\zeta}{Mc_m^{(4)}(0)\int_0^{\pi}[ce_m(\zeta)d\zeta]}\ ^\dagger$$

and $\quad f(\cos\zeta) = e^{-i\nu\cos\zeta}\int_{\infty}^{1-\cos\zeta} e^{-i\nu\xi}H_0^{(2)}(\kappa\xi)\ d\xi\ ^\ddagger$

(3.44)

The circulatory lift amplitude have the form

$$\overline{L}^{(2)}|_{Haskind} = 2\rho_o U \sum_{m=0}^{\infty} \int_0^{\pi} e^{-i\mu\cos\zeta} \left[A\alpha_+^m + B\alpha_-^m\right] d\zeta \tag{3.45}$$

A second equation relating A and B was obtained by satisfying trailing edge finite velocity.

* A minus sign is omitted from the exponential term in the second bracket in Haskind [27] original formulation.

† This expression is reformulated to cancel normalization.

‡ Analytical solution of the infinite integral in the Appendix C

Chapter 4

Computational Simulation

In this chapter, we illustrate the computational set-up used in investigating the effect of compressibility on the aerodynamic loads using Navier-Stokes simulations to support the theoretical results. The computations were implemented using the software package ANSYS FLUENT 20.1. As viscosity effect is beyond the scope of the present study, inviscid flow model have been considered. For the compressible inviscid flow model, FLUENT solves Euler equations and ideal gas low is used for coupling between momentum and energy equations.

Note that aerodynamic theories developed in chapter 3 assumes a potential barotropic fluid where the vorticity is zero and the density is a function of pressure only. Hence, the baroclinic term $\frac{1}{\rho_o^2}\nabla \mathbf{p}_o \times \nabla \rho_o$ in the vorticity equation 1.4 vanishes. However, the inviscid flow model in ANSYS FLUENT assumes non-barotropic fluid. This inconsistency is believed to result in a phase difference between theoretical and computational aerodynamic loads. Nevertheless, the inviscid model is sufficient to validate and support the theoretical results.

4.1 Computational Grid

The flat plate have a chord length of 1 m and a thickness of 10^{-4} c. The theories assumes a zero thickness plate but a thickness was added to avoid the existence of high aspect ratio cells in the far field region. The present work involves high Mach numbers and high frequencies, so the leading and the trailing edges were carefully designed as shown in figure 4.1 to avoid the existence of supersonic flow near the plate edges.

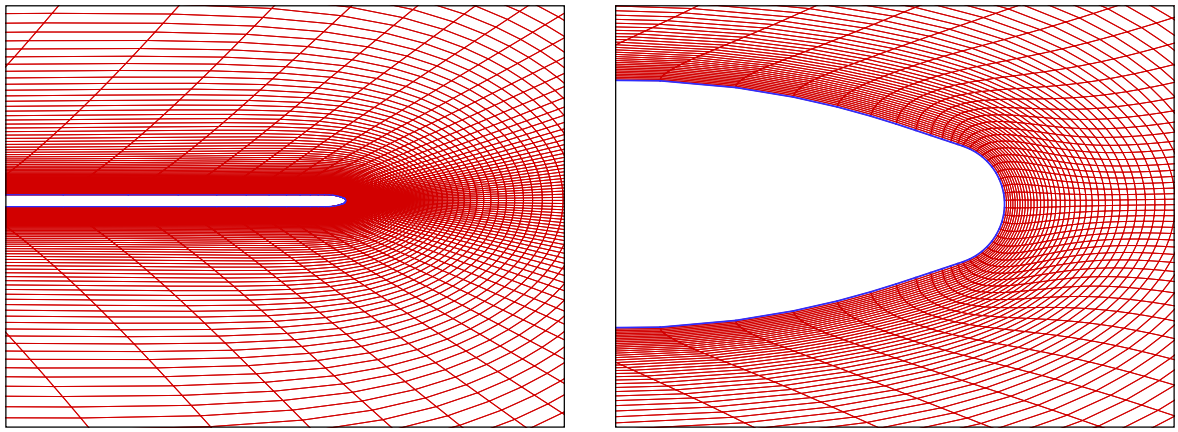

(a) **(b)**

Figure 4.1: (a) mesh elements around the upper surface, lower surface and near the wake region. (b) Near trailing edge mesh illustrating mesh orthogonality and quality.

A two dimensional structured O-grid is generated using ICEM CFD package. The computational domain is divided into three zones (rings) as illustrated in figure 4.2. The inner ring(red), surrounding the plate, has a radius of 5 c. The mesh in this region is dense to capture the flow characteristics and the pressure waves traveling to the far field. The first cell height was set to 10^{-6} c with expansion ratio 1.1. A total number of 320 mesh elements were utilized on both the upper and lower surfaces of the plate and 180 cell elements around both the leading and trailing edges.

To maintain a high quality mesh near the flat plate surface during motion, the inner ring and the flat plate move as a rigid body performing plunging motion using a user defined

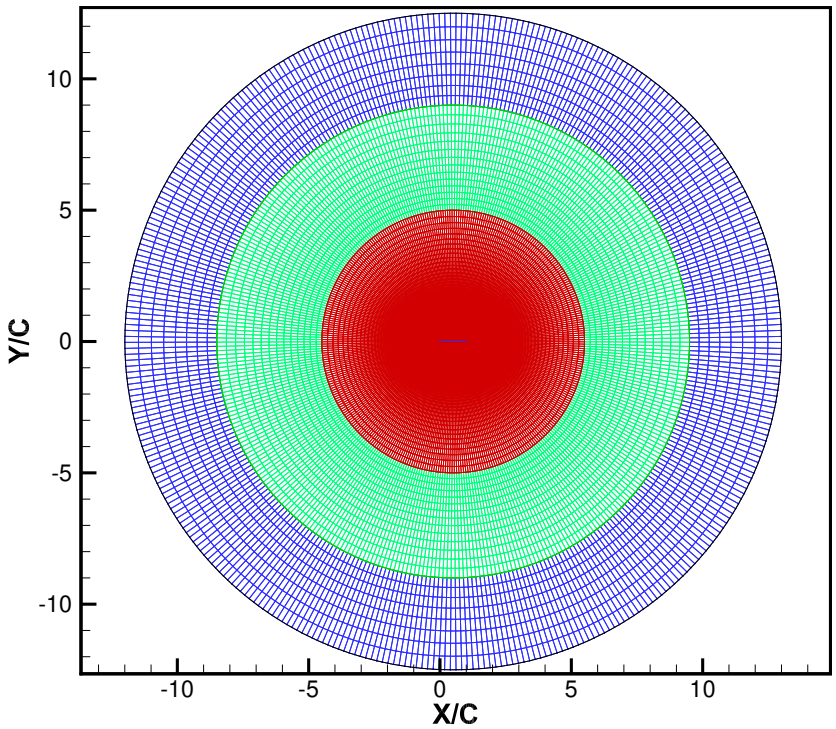

Figure 4.2: Two dimensional O-grid mesh showing the complete computational domain. Outer zone (blue) is stationary and the pressure far field defiled at the outer boundary. Intermediate zone (green) deforms to absorb the plate motion. Inner zone (red) moved as a rigid body.

function (UDF). The outer ring (blue) has a far field (outer) radius of 12.5 c and an inner radius of 9 c. This ring is stationary to insure an accurate implementation of the outer boundary condition. The intermediate ring (green) has a main role in absorbing the motion of the inner ring. Remeshing and deforming techniques are used for the intermediate zone to accurately deform and to avoid bad elements quality.

4.2 Solver Set-Up

Regarding the solver set-up, the pressure far field boundary condition was selected for the outer boundary. The density based solver was considered for compressible flow with implicit formulation. As mentioned in the chapter introduction, the inviscid flow model was adopted

for all the simulations. Green-Gauss Node Based (GGNB) scheme was selected spatial gradient discretization. Despite its computational cost, the GGNB scheme provide the highest accuracy for variables gradient computations. Second order implicit scheme for the transient formulation was designated. A total number of 300 time steps per cycle was maintained for all computations ensuring a converged solution for all variables. To obtain a faster solution convergence, a steady-state solution was used to initialize the transient solution.

Chapter 5

Results

The aerodynamic loads and the frequency response functions of a flat plate performing plunging motions in compressible flow are presented in this chapter for three Mach number values; $M = 0.35, 0.5$ and 0.6.

5.1 Validation

Before proceeding to determine the compressible aerodynamic loads, the theoretical results and the CFD simulations need to be validated. The normalized plunging lift magnitude at $M = 0.5$ corresponding to Haskind [27], Reissner [26] and CFD simulations are compared to the previously given results by Timman [32] and Amiet [57]. As shown in figure 5.1, the CFD results shows and excellent agreement to the analytical results by Timman for the entire presented frequency range. The difference between all the compared results tend to decrease as the reduced frequency increase. From the figure it can be noticed that in opposition to Timman's and Amiet's lift computations, Reissner's and Haskind's results encounter spurious rapid oscillations. The cause of these oscillations isn't, yet, fully understood.

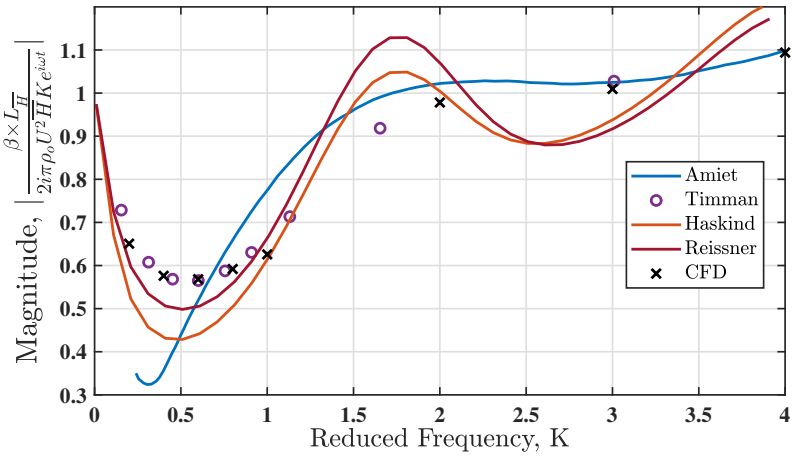

Figure 5.1: Normalized total plunging lift magnitude by Haskind [27], Reissner [26] and CFD simulations compared to previous results by Timman [32] and Amiet [57]. The results were computed at $M = 0.5$. The present theoretical and computational results shows a good agreement to the previous counterparts.

5.2 Total Lift

The plate is plunging harmonically with amplitude $\overline{H} = 2 \times 10^{-3}$ and positive direction upward. The normalized lift and phase angle corresponding to Haskind's [27] and Reissner's [26] formulations are shown in figure 5.2 in comparison to the compressible lift by Theodorsen [8]. The general subsonic, compressible, Theodorsen lift function is obtained by employing the famous Prandtl-Glauert transformation. Intuitively, as the Mach number increase, the lift magnitude decrease. For small frequencies, the lift and phase approach Theodorsen incompressible lift and phase. Hence, the compressibility has an imperceptible effect on the aerodynamic loads for low frequency values. Interestingly, this discovery supports the conclusion of an earlier effort by Mazelsky [29]. He computed the aerodynamic loads for oscillating rectangular and delta winds in compressible flow for a wide range of reduced frequencies. The lift and phase are independent of the reduced frequency for high frequency values.

The CFD lift amplitude and phase shows a good agreement to the theoretical counterpart. The present findings are critical in flutter analysis [58, 59], design of gas turbine

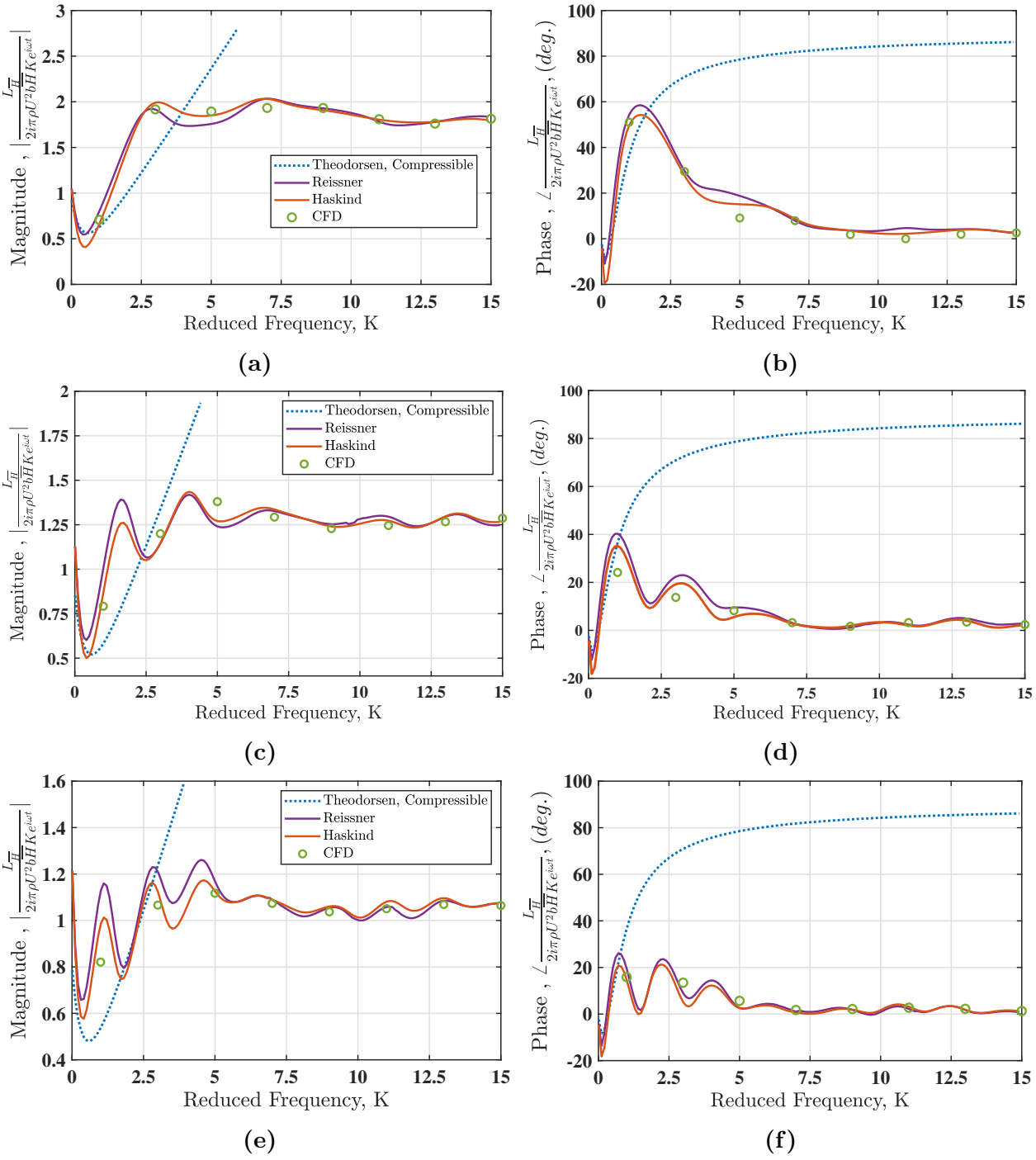

Figure 5.2: Theoretical results of the Normalized total lift $L_{\overline{H}}$ and phase due to plunging at different Mach numbers are compared to computational and incompressible results. The computational results supports the theoretical results and showing a reduction in amplitude and phase lag with increasing Mach number. (a) and (b) Plunging at $M = 0.35$. (c) and (d) Plunging at $M = 0.5$. (e) and (f) Plunging at $M = 0.6$.

blades [60, 61] and high flexible wings. Theodorsen [8] compressible analysis can't,correctly, predict the significant phase difference between the aerodynamic loads and the plate motion. These findings supports our discussion in chapter 1, that Prandtl-Glauert transformation is insufficient for extending the unsteady incompressible theories to account for compressibility effects. Hence, it's recommended to use Haskind's [27] and Reissner's [26] models for a better estimation of aerodynamic loads and flutter boundary in compressible flow.

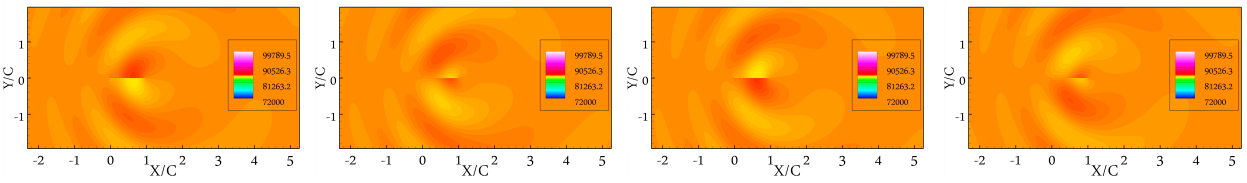

$H = 0, \quad \dot{H} > 0$ $H = 10^{-3}m, \ \dot{H} = 0$ $H = 0, \quad \dot{H} < 0$ $H = -10^{-3}m, \ \dot{H} > 0$

Figure 5.3: Pressure contours of a harmonically plunging plate at $M = 0.5$ and $K = 3$. The plate forms a single dipole source with wavelength $\frac{\lambda_a}{2b} = 2$.

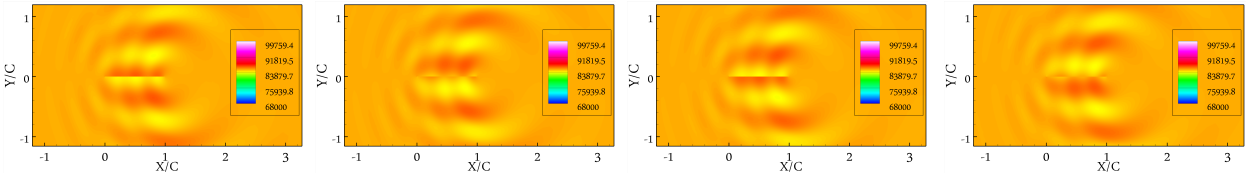

$H = 0, \quad \dot{H} > 0$ $H = 10^{-3}m, \ \dot{H} = 0$ $H = 0, \quad \dot{H} < 0$ $H = -10^{-3}m, \ \dot{H} > 0$

Figure 5.4: Pressure contours of a harmonically plunging plate at $M = 0.5$ and $K = 9$. Three dipole sources are present along the plate surface.

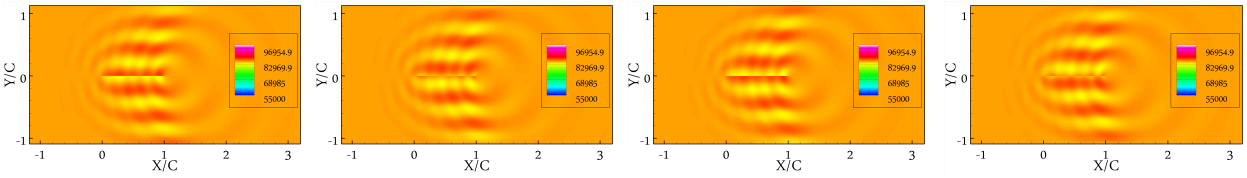

$H = 0, \quad \dot{H} > 0$ $H = 10^{-3}m, \ \dot{H} = 0$ $H = 0, \quad \dot{H} < 0$ $H = -10^{-3}m, \ \dot{H} > 0$

Figure 5.5: Pressure contours of a harmonically plunging plate at $M = 0.5$ and $K = 15$. A total number of five dipole sources are present along the plate surface with short wavelength.

Figures 5.3 - 5.5 show the contours of the traveling pressure waves around the flat plate at selected oscillation cycle times at $M = 0.5$. As shown in figure 5.3, the plate forms a single

dipole source radiating pressure waves of wave length $\frac{\lambda_a}{2b} \approx 2$. This result agrees to the classical aerodynamic noise theory where the plate surface forms a dipole source if its chord is small compared to the wavelength [62, 63]. Figures 5.4 and 5.5 clearly show that as the oscillation frequency increase, the wave length decrease and the number of dipole sources distributed along the plate surface increase.

Interestingly, it can be inferred from the previous results and discussion that as the number of dipole sources, distributed along the plate chord, increase (wave length decrease), the phase difference between the aerodynamic loads and the plate motion decrease. In the context of the aerodynamics noise theory, it's convenient to split the domain of oscillation frequency into three sections. In the first section, the wave length is large and the fluid around the airfoil is considered incompressible. For the second section, where plate acts as a single dipole source and the phase difference is significant. Finally, the third section have a small phase lag and the plate utilizes multiple dipole sources. Based on the simulation results of the three Mach numbers, It's important to mention that as M increase, the upper frequency limit of the first two sections decrease and the lower limit of the third section increase.

Before proceeding to investigate the compressible circulatory and non-circulatory frequency response, it's important to discuss some recent developments concerning this classification. The classification of the unsteady aerodynamic lift into circulatory and non-circulatory components was introduced by Theodorsen [8]. Since then, this classification was used by the pioneers in their research and was extended to account for compressibility and viscosity effects [26, 27, 64, 65, 66]. The non-circulatory component designate the force required to move (accelerate) the airfoil and its surrounding air and corresponds to flow without circulation. To satisfy the Kutta condition at the trailing edge, circulatory component was added. Taha [10], intensively discussed this classification and pointed out that the circulatory lift isn't lift due to circulation and showed a phase lag between the development of the circulatory lift and circulation in the case of potential flow. He showed the deficiency of

Theodorsen function to represent a real dynamical system. Taha also manifested that the non-circulatory component encounters some circulation due to viscosity resulting in a phase difference between CFD computations and Theodorsen predictions.

5.3 Compressible Circulatory Lift Frequency Response Function

The transfer function defined as the ratio of the circulatory lift to the quasi-steady lift is usually declared as circulatory lift frequency response function. As the simulation results are expressed as a time history of the total lift, we adopt the procedure followed by Taha [66] in determining the viscous lift frequency response function. Taha extended the unsteady inviscid aerodynamic theory to account for viscosity and showed that viscosity induces a higher phase lag compared to Theodorsen's [8] estimation. Fourier transform is utilized to express the total lift in a complex form $\hat{L_{\overline{H}}}$. Using Reissner's [26] prediction of the non-circulatory lift (3.28), the circulatory lift is obtained by subtracting the non-circulatory lift from the total lift. In the case of plunging motion, the quasi-steady lift have the form $L_{QS} = 2\pi i \rho_o U^2 b K \overline{H} e^{i\omega t}$. Finally, the resulting circulatory lift is divided by the quasi-steady lift to obtain the compressible frequency response function $C_v(K) = L_{C,\overline{H}}/L_{QS}$.

Figure 5.6 shows the compressible circulatory lift frequency response for two different Mach numbers, $M = 0.35$ and $M = 0.6$ using Reissner's [26] and Haskind's [27] formulations. Figure 5.6 also shows the general Theodorsen [8] lift frequency response function and CFD results for comparison. The frequency response function magnitude decrease as M increase and K increase. In other words, the high frequency gain K_{hf} decrease as M increase. The CFD results agree to the theoretical results in magnitude and phase and shows a significant phase difference compared to Theodorsen results.

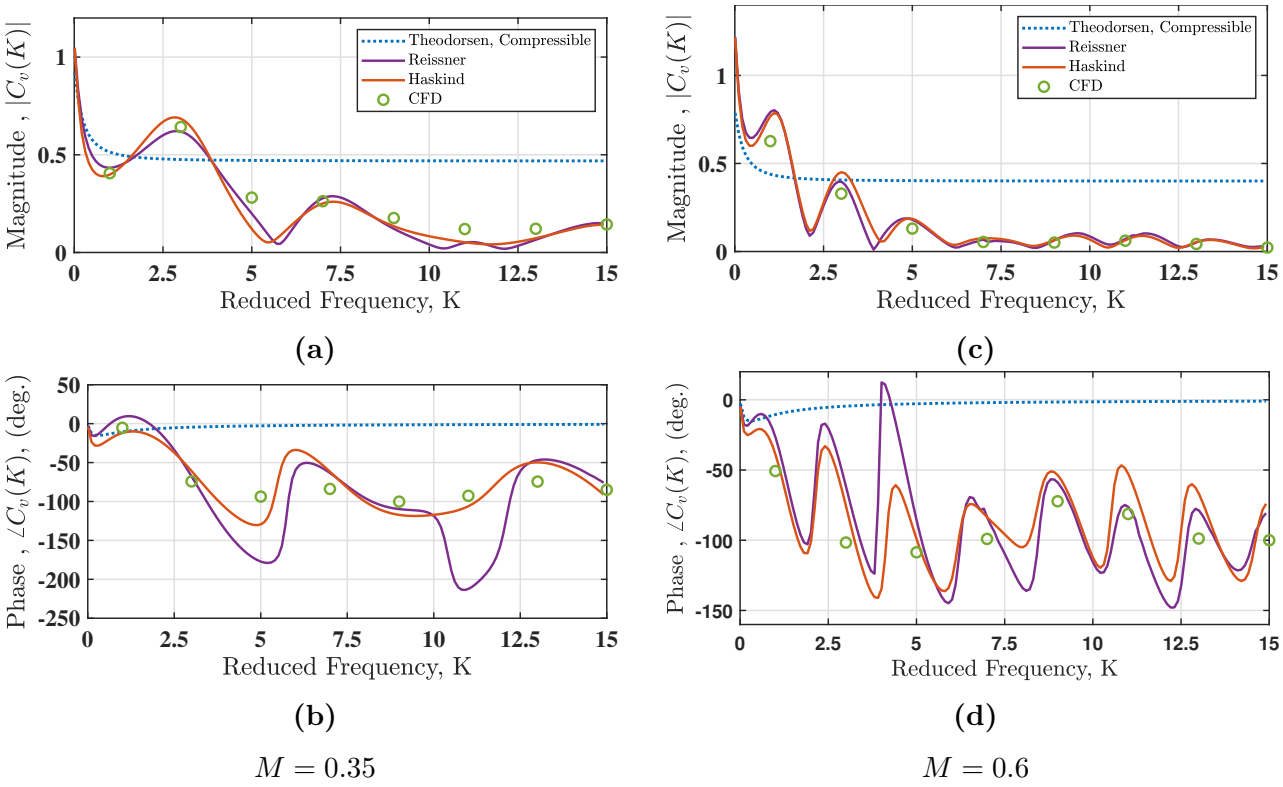

Figure 5.6: (Solid lines) Theoretical circulatory frequency response function compared to Theodorsen [8] and CFD results at different Mach numbers. The high frequency gain and phase lag are notably different from Theodorsen prediction.

5.4 Compressible Non-Circulatory Frequency Response Function

According to the unsteady, inviscid, incompressible aerodynamic theory, the noncirculatory loads responds instantaneously to the airfoil motion with a constant 90^o phase difference. In the context of the present research, it would be interesting to study the effect of compressibility on the non-circulatory lift. As stated by Theodorsen [8], the non-circulatory loads in the case of plunging motion can be expressed as $L_{NC,\overline{H}} = \pi\rho b^2 \ddot{H}$. Figure 5.7 shows a time history of Reissner's [26], compressible, lift computation compared to Theodorsen, incompressible, counterpart. As shown in the figure, compressibility triggers a phase lag (dynamics) between the lift generation and the airfoil motion compared to Theodorsen's lift.

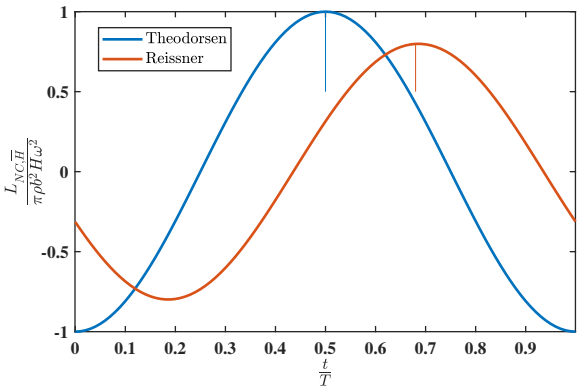

Figure 5.7: Comparison between Theodorsen [8] non-circulatory lift and Reissner computations. The lift is normalized by the maximum lift. This cycle is computed at $M = 0.5$ and $K = 3$.

Figure 5.8 shows a the non-circulatory, compressible, transfer function at different Mach numbers. As Reissner and Haskind formulations regarding the non-circulatory loads are identical, Reissner [26] results are only presented. Similar to circulatory frequency response function , the magnitude of non-circulatory frequency function decrease as M increase. The phase lag is remarkable at low reduced frequencies. It's interesting to notice that The phase lag is almost independent of k for $k > 10$ regardless of the Mach number value.

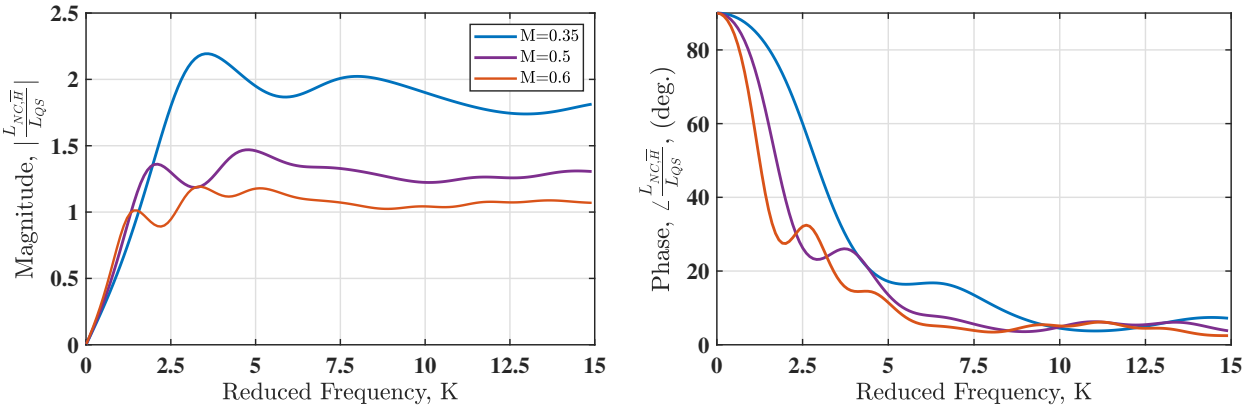

Figure 5.8: Compressible non-circulatory frequency response function and phase at different Mach numbers using Reissner [26] formation. The magnitude of the transfer function decrease as M increase.

Chapter 6

Conclusion and Future Work

6.1 Conclusion

The present thesis provided some fundamental understanding of the unsteady loads in compressible flow. The literature review in chapter 1 showed that deep understanding of the aerodynamic loads in unsteady compressible flow isn't well established. Reissner and Haskind provided unsteady, compressible, models that can distinguish between the circulatory and the non-circulatory contributions. From the results presented in chapter 5, we have the following conclusions

1. The total lift magnitude decreases as the Mach number increases. The compressibility effect is trivial for small frequency values. However, the compressibility effect is significant at high frequencies. Contrary to incompressible aerodynamic theories, the total lift phase approaches zero for large reduced frequency.

2. Using Prandtl-Glauert transformation to generalize the unsteady, incompressible, theories fails to capture the significant phase difference between the aerodynamic loads

and the plate motion.

3. Radiating pressure waves of wavelength larger than the plate chord, the oscillating plate acts as a single dipole source and encounters a remarkable phase lag. As the frequency increases, the number of dipole sources, distributed along the plate chord, increase and the associated phase lead decreases.

4. The circulatory lift frequency response function magnitude decreases, and its dc gain increases as M increases. The function magnitude is independent of k for high reduced frequency values.

5. The non-circulatory lift transfer function encounters a notable phase lag at high K values.

6.2 Future Work

The fundamental concepts and ideas discussed in this thesis can assist to form a basis for future research. It would be interesting to extend the two-dimensional theory to consider the span wise effects. Capturing the amount of energy radiated to infinity using conservation of energy principle can improve the understanding of the pressure waves nature.

Viscosity will, definitely, induce additional phase lag. So, extending the theory to account for viscosity can estimate a more accurate flutter boundary and allows for investigating the free stream turbulence on the aerodynamic loads. Finally, it's important to investigate the impact of different degrees of motion on the aerodynamic loads.

Bibliography

[1] Frank M White and Joseph Majdalani. *Viscous fluid flow*, volume 3. McGraw-Hill New York, 2006.

[2] Roger D Blandford and Kip S Thorne. Applications of classical physics. *lecture notes, California Institute of Technology*, page 12, 2008.

[3] John David Anderson Jr. *Fundamentals of aerodynamics*. Tata McGraw-Hill Education, 2010.

[4] CC Lin, Eric Reissner, and HS Tsien. On two-dimensional non-steady motion of a slender body in a compressible fluid. *Journal of Mathematics and Physics*, 27(1-4):220–231, 1948.

[5] John W Miles. Linearization of the equations of non-steady flow in a compressible fluid. *Journal of Mathematics and Physics*, 33(1-4):135–143, 1954.

[6] MJ Lighthill. A new approach to thin aerofoil theory. *Aeronautical Quarterly*, 3(3):193–210, 1951.

[7] Milton D. Van Dyke. A study of hypersonic small disturbance theory. Technical Report 3173, NACA, May 1954.

[8] Theodore Theodorsen and WH Mutchler. General theory of aerodynamic instability and the mechanism of flutter. Technical Report 496, NACA, 1935.

[9] Ülgen Gülçat. *Fundamentals of modern unsteady aerodynamics*. Springer, Cham, Switzerland, 2021.

[10] Haitham E Taha and Amir S Rezaei. On the dynamics of unsteady lift and circulation and the circulatory-non-circulatory classification. In *AIAA Scitech 2019 Forum*, page 1853, 2019.

[11] WP Jones. Oscillating wings in compressible subsonic flow. Technical Report R.M 2855, British Aeronautical Research Council, London,England, October 1951.

[12] John W Miles. Quasi-stationary airfoil theory in subsonic compressible flow. *Quarterly of Applied Mathematics*, 8(4):351–358, 1951.

[13] A.I. Van De Vooren. Unsteady airfoil theory. In *Advances in Applied Mechanics*, volume 5, pages 35–89. Elsevier, 1958.

[14] Camillo Possio. L'azione aerodinamica sul profilo oscillante in un fluido compressibile a velocita iposonora. *L'aerotecnica*, 18(4):441–458, 1938.

[15] R.A Frazer and Sylvia W. Skan. Possio's subsonic derivative theory and its application to flexural-torsional wing flutter parts 1. Technical Report 2553, ARC-RM, London, England, 1951.

[16] Th Schade. Numerical solution of the possio integral equation of the oscillating aerofoil in a two-dtiensional subsonic flow. part iv-numerical part. reps. and translations no. 846. *British MAP V61kenrode*, 1947.

[17] Dietze. The air forces for the harmonically oscillating aerofoil in a compressible medium at subsonic speeds: Two-dimensional problem. *ARC*, 10(219), 1946.

[18] Kussner H.G. General airfoil theory. Technical Report 979, NACA, 1941.

[19] L. Prandtl. General considerations on the flow of compressible fluids. Technical Report 805, NACA, 1936.

[20] John W Miles. A note on a solution of possio's integral equation for an oscillating airfoil in subsonic flow. *Quarterly of Applied Mathematics*, 7(2):213–216, 1949.

[21] Charles E Watkins, Harry L Runyan, and Donald S Woolston. *On the kernel function of the integral equation relating the lift and downwash distributions of oscillating finite wings in subsonic flow*, volume 1234. National Advisory Committee for Aeronautics, 1954.

[22] IT Minhinnick. Subsonic aerodynamic flutter derivatives for wings and control surfaces (compressible and incompressible flow. Technical Report 87, British R.A.E, 1950.

[23] W Prichard Jones. The oscillating aerofoil in subsonic flow. Technical Report R.M 2921, Aeronautical Research Council, 1953.

[24] Reinier Timman. *Beschouwingen over de luchtkrachten op trillende vliegtuigvleugels*. PhD thesis, Technische Hogeschool te Delft, Delft, Netherlands, 1946.

[25] Reinier Timman and Adriaan Isak Van de Vooren. *Theory of the Oscillating Wing with Aerodynamically Balanced Control Surface in a Two-Dimensional, Subsonic, Compressible Flow*. Nationaal Luchtvaartlaboratorium, 1949.

[26] Eric Reissner. On the application of mathieu functions in the theory of subsonic compressible flow past oscillating airfoils. Technical Report 2363, NACA, Washington,USA, May 1951.

[27] MD Haskind. Oscillations of a wing in a subsonic gas flow. prikl. mat. i mekh. moskow xi, 1, 129–146 (1947). *Russian Air Material Command and Brown Univ. Translation A9-T*, 22.

[28] A.E Billington. Harmonic oscillations of an aerofoil in subsonic flow. Technical Report A 65, Australian Aeronautical Research Lab, Australia, 1949.

[29] Bernard Mazelsky. Theoretical aerodynamic properties of vanishing aspect ratio harmonically oscillating rigid airfoils in a compressible medium. *Journal of the Aeronautical Sciences*, 23(7):639–652, 1956.

[30] DJ Hofsommer. Systematic representation of aerodynamic coefficients of an oscillating aerofoil in two-dimensional incompressible flow. Technical Report F 61, NLL, 1950.

[31] HG Küssner. A general method for solving problems of the unsteady lifting surface theory in the subsonic range. *Journal of the Aeronautical Sciences*, 21(1):17–26, 1954.

[32] R Timman, AI Van de Vooren, and JH Greidanus. Aerodynamic coefficients of an oscillating airfoil in two-dimensional subsonic flow. *Journal of the Aeronautical Sciences*, 18(12):797–802, 1951.

[33] F Dietze. Die luftkräfte des harmonisch schwingenden flügels im kompressiblen medium bei unterschallgeschwindigkeit. *DVL Forschungsbericht 1733*, 1943.

[34] R Timman. Linearized theory of the oscillating airfoil in compressible subsonic flow. *Journal of the Aeronautical Sciences*, 21(4):230–236, 1954.

[35] Henry E Fettis. Comments on aerodynamic coefficients of an oscillating airfoil in two-dimensional subsonic flow. *Journal of the Aeronautical Sciences*, 19(5):353–354, 1952.

[36] SA Schwarz. Application of a semi-empirical sputtering model to secondary electron emission. *Journal of applied physics*, 68(5):2382–2391, 1990.

[37] W. P. Jones. Aerofoil oscillations at high mean incidences. Technical Report 2654, ARC-RM, 1948.

[38] Earll M Murman and Julian D Cole. Calculation of plane steady transonic flows. *AIAA journal*, 9(1):114–121, 1971.

[39] WF Ballhaus and PM Goorjian. Implicit finite-difference computations of unsteady transonic flows about airfoils. *AIAA Journal*, 15(12):1728–1735, 1977.

[40] Jichao Su and Behrouz Tabarrok. A time marching integral equation method for unsteady state problems. *Computer methods in applied mechanics and engineering*, 142(3-4):203–214, 1997.

[41] Robert Mazet. *Manual on Aeroelasticity*, volume 6. AGARD, 1968.

[42] G Bicken and GF Carey. *Harmonic Small Perturbation Computation for Sinusoidal Lift Response*. Texas Institute for Computational and Applied Mathematics, University of Texas at Austin, 1996.

[43] Sydney Goldstein. *Mathieu functions*. PhD thesis, University of Cambridge, United Kingdom, 1928.

[44] EL Ince. Xxii.—tables of the elliptic-cylinder functions. *Proceedings of the Royal Society of Edinburgh*, 52:355–423, 1933.

[45] Julls Adams Stratton. Electromagnetic theory, mcgrow-hill book company. *Inc., New York, and London*, 1941.

[46] Philip M Morse and Herman Feshbach. Methods of theoretical physics. *American Journal of Physics*, 22(6):410–413, 1954.

[47] G Blanch. Mathieu functions, handbook of mathematical functions. *Ed, by M. Abramowitz and I, A, Stegun, National Bureau of Standards, U. S, Government Printing Office, Washington, DC*, 1968.

[48] Group "Numerical Analysis" at Delft University of Technology. On the computation of mathieu functions. *Journal of Engineering Mathematics*, 7:39–61, 1973.

[49] Cojocaru, E. Mathieu functions computational toolbox implemented in matlab. `https://arxiv.org/abs/0811.1970`, 2008. arXiv–0811.

[50] Julio C Gutiérrez-Vega, RM Rodrıguez-Dagnino, MA Meneses-Nava, and S Chávez-Cerda. Mathieu functions, a visual approach. *American Journal of Physics*, 71(3):233–242, 2003.

[51] Malcolm M Bibby and Andrew F Peterson. Accurate computation of mathieu functions. *Synthesis Lectures on Computational Electromagnetics*, 8(2):1–133, 2013.

[52] Howard B Wilson and Robert W Scharstein. Computing elliptic membrane high frequencies by mathieu and galerkin methods. *Journal of Engineering Mathematics*, 57(1):41–55, 2007.

[53] AK Hamid, MI Hussein, HA Ragheb, and M Hamid. Mathieu functions of complex argument and their applications to the scattering by lossy elliptic cylinders. *Applied Computational Electromagnetics Society Journal*, 17(3):209, 2002.

[54] Norman William McLachlan. *Theory and application of Mathieu functions*. Publisher to the University Geoffrey Cumberlege, Oxford University Press, 1951.

[55] Arnie Van Buren and Jeffrey Boisvert. Accurate calculation of the modified mathieu functions of integer order. *Quarterly of applied mathematics*, 65(1):1–23, 2007.

[56] Milton Abramowitz, Irene A Stegun, and Robert H Romer. *Handbook of mathematical functions with formulas, graphs, and mathematical tables*. American Association of Physics Teachers, Maryland, 1988.

[57] Roy K Amiet. High frequency thin-airfoil theory for subsonic flow. *AIAA journal*, 14(8):1076–1082, 1976.

[58] Mohamed Y Zakaria, Mohammad Y Al-Haik, and Muhammad R Hajj. Experimental analysis of energy harvesting from self-induced flutter of a composite beam. *Applied Physics Letters*, 107(2):023901, 2015.

[59] Ahmed A Hussein and Robert A Canfield. Unsteady aerodynamic stabilization of the dynamics of hingeless rotor blades in hover. *AIAA Journal*, 56(3):1298–1303, 2018.

[60] A.V Srinivasan. Flutter and resonant vibration characteristics of engine blades. *Journal of engineering for gas turbines and power*, 119(4):742–775, 1997.

[61] AA Mikolajczak, RA Arnoldi, LE Snyder, and H Stargardter. Advances in fan and compressor blade flutter analysis and predictions. *Journal of Aircraft*, 12(4):325–332, 1975.

[62] N Curle. The influence of solid boundaries upon aerodynamic sound. *Proceedings of the Royal Society of London. Series A. Mathematical and Physical Sciences*, 231(1187):505–514, 1955.

[63] Hanno H Heller and Sheila E Widnall. Sound radiation from rigid flow spoilers correlated with fluctuating forces. *The Journal of the Acoustical Society of America*, 47(3B):924–936, 1970.

[64] Harvard Lomax, Max A Heaslet, Franklyn B Fuller, and Loma Sluder. Two-and three-dimensional unsteady lift problems in high-speed flight. Technical Report 1077, NACA, 1952.

[65] JG Leishman. Indicial lift approximations for two-dimensional subsonic flow as obtained from oscillatory measurements. *Journal of Aircraft*, 30(3):340–351, 1993.

[66] Haithem Taha and Amir S Rezaei. Viscous extension of potential-flow unsteady aerodynamics: the lift frequency response problem. *Journal of Fluid Mechanics*, 868:141–175, 2019.

Appendix A

Derivation of Coefficient I_m in Eqn. 3.31

$$
\begin{aligned}
I_m = \int_0^{\pi} e^{-i\mu\cos\zeta}\sin\zeta\ se_m(\zeta)\ d\zeta &= \frac{1}{2}\sum_{n=1}^{\infty} B_{mn}\int_0^{\pi} e^{-i\mu\cos\zeta}\left[\cos(n-1)\zeta - \cos(n+1)\zeta\right] \\
&= \frac{\pi}{2}\sum_{n=1}^{\infty} B_{mn}\left[-i^{(n+1)}J_{n-1}(-\mu) - i^{(n+1)}J_{n+1}(-\mu)\right] \\
&= \frac{\pi}{2}\sum_{n=1}^{\infty} B_{mn}\ \ i^{(n+1)}\left[\frac{2n}{\mu}J_n(-\mu)\right] \\
&= \frac{\pi}{\mu}\sum_{n=1}^{\infty} n\ (-1)^n\ i^{(n+1)}J_n(\mu)
\end{aligned}
\tag{A.1}
$$

Appendix B

Analytical Solution of The Infinite Integral in Eqn. 3.38

The solution of the integral $\int_0^\infty e^{-i\nu\cosh\zeta} Mc_m^{(4)}(\zeta)\sinh\zeta \ d\zeta$ will Begin by expressing Radial mathieu equation of the forth kind in terms of hankel function of the second kind. The integral will then have the form

$$\int_0^\infty e^{-i\nu\cosh\xi} Mc_m^{(4)}(\xi)\sinh\xi \ d\xi = \sum_{r=0}^{\infty}(-1)^r A_r^{(n)} \int_0^\infty e^{-i\nu\cosh\xi} H_r^{(2)}(2\sqrt{q}\cosh\xi) \ \sinh\xi \ d\xi \tag{B.1}$$

Changing the variables to be expressed as $u = \cosh\xi, \ du = -\sinh\xi \ d\xi$. Equation B.1 will be as follows

$$\int_0^\infty e^{-i\nu\cosh\xi} Mc_m^{(4)}(\xi)\sinh\xi \ d\xi = -\sum_{r=0}^{\infty}(-1)^r A_r^{(n)} \int_0^\infty e^{-i\nu \ u} H_r^{(2)}(2\sqrt{q} \ u) \ \ du \tag{B.2}$$

Hankel function can be expressed as a linear summation of bessel functions as

$$H_r^{(2)} = J_r(z) - i \ Y_r(z) \tag{B.3}$$

where

$$J_r(z) = \left(\frac{z}{2}\right)^r \sum_{k=0}^{\infty} (-1)^k \frac{\left(\frac{z^2}{4}\right)^k}{k!\ \Gamma(r+k+1)} \tag{B.4}$$

$$\begin{aligned} Y_r(z) = &-\frac{(z/2)^{-r}}{\pi} \sum_{k=0}^{r-1} \frac{(r-k-1)!}{k!} \left(\frac{z^2}{4}\right)^k + \frac{2}{\pi} \ln\left(\frac{z}{2}\right)\ J_r(z) \\ &-\frac{(z/2)^r}{\pi} \sum_{k=0}^{\infty} [\psi(k+1) + \psi(r+k+1)] \frac{\left(\frac{-z^2}{4}\right)^k}{k!\ (r+k)!} \end{aligned} \tag{B.5}$$

Substituting Eqns.[B.3-B.5] into Eqn. B.2 and for simplicity the resulting terms will be referred to as I_1, I_2, I_3 *and* I_4 respectively.

$$\begin{aligned} I_1 &= \int_0^{\infty} e^{-i\nu u} \left[(\sqrt{q}u)^r \sum_{k=0}^{\infty} (-1)^k \frac{(qu^2)^k}{k!\ \Gamma(r+k+1)!} \right] du \\ &= (\sqrt{q})^r \sum_{k=0}^{\infty} (-1)^k \frac{(\sqrt{q})^{2k}}{k!\ \Gamma r + k + 1} \int_0^{\infty} e^{-i\nu u} u^{r+2k} du \\ &= (\sqrt{q})^r \sum_{k=0}^{\infty} (-1)^k \frac{(\sqrt{q})^{2k} \Gamma(r+2k+1)}{k!\ \Gamma(r+k+1)\ (i\nu)^{(r+2k+1)}} \end{aligned} \tag{B.6}$$

$$\begin{aligned} I_2 &= \int_0^{\infty} e^{-i\nu u} \left[\frac{(\sqrt{q}u)^{-r}}{\pi} \sum_{k=0}^{r-1} \frac{(r-k-1)!\ (qu^2)^2}{k!} \right] du \\ &= \frac{(\sqrt{q})^{-r}}{\pi} \sum_{k=0}^{r-1} \frac{(r-k-1)!}{k!} (q)^k \int_0^{\infty} e^{-i\nu u} u^{2k-r} \\ &= \frac{(\sqrt{q})^{-r}}{\pi} \sum_{k=0}^{r-1} \frac{(\sqrt{q})^{2k} (r-k-1)!\ \Gamma(2k-r+1)}{k!\ (i\nu)^{(2k-r+1)}} \end{aligned} \tag{B.7}$$

where $r > 1$. Convergence limit for Eqn. B.7 is $|i\nu| > |\sqrt{q}|$.

$$\begin{aligned} I_3 &= \frac{2}{\pi}\int_0^\infty e^{-i\nu u}\ln(\sqrt{q}u)\left[(\sqrt{q}u)^r\sum_{k=0}^{\infty}\frac{(-1)^k(qu^2)^k}{k!\Gamma(r+k+1)}\right]du \\ &= \frac{2(\sqrt{q})^r}{\pi}\sum_{k=0}^{\infty}\frac{(-1)^k(\sqrt{q})^{2k}}{k!\ \Gamma(r+k+1)}\int_0^\infty e^{-i\nu u}\ln(\sqrt{q}u)\ u^{(r+2k)} \\ &= \frac{2(\sqrt{q})^r}{\pi}\sum_{k=0}^{\infty}\frac{(-1)^k(\sqrt{q})^{2k}}{k!\ \Gamma(r+k+1)}\left[\frac{\ln(\sqrt{q})\Gamma(r+2k+1)}{(i\nu)^{(r+2k+1)}}+\int_0^\infty e^{-i\nu u}\ln(u)\ u^{(r+2k)}du\right] \end{aligned} \tag{B.8}$$

Introducing a change of variables to the infinite integral in the form

$$let \quad R = i\nu u, \quad u = -\frac{iR}{\nu}, \quad du = -\frac{i}{\nu}dR \tag{B.9}$$

Using Eqn. B.9

$$\begin{aligned} &\int_0^\infty e^{-i\nu u}\ln(u)\ u^{(r+2k)}du = \left(\frac{-i}{\nu}\right)^{(r+2k)+1}\int_0^\infty e^{-R}\ln\left(\frac{R}{i\nu}\right)R^{(r+2k)}\ dR \\ &= \left(\frac{-i}{\nu}\right)^{(r+2k+1)}\left[\Gamma'(r+2k+1)-\ln\left(\frac{-i}{\nu}\right)\Gamma(r+2k+1)\right] \end{aligned} \tag{B.10}$$

where Γ' is the derivative of Gamma function. Substituting Eqn. B.10 into Eqn. B.8, I_3 will be in the form

$$\begin{aligned} I_3 = \frac{2(\sqrt{q})^r}{\pi}\sum_{k=0}^{\infty}&(-1)^k\frac{(\sqrt{q})^{2k}\Gamma(r+2k+1)}{k!\ \Gamma(r+k+1)} \\ &\left[\frac{\ln(\sqrt{q})}{(i\nu)^{r+2k+1}}+\left(\frac{-i}{\nu}\right)^{(r+2k+1)}\left(\psi(r+2k+1)-\ln\left(\frac{-i}{\nu}\right)\right)\right] \end{aligned} \tag{B.11}$$

$$\begin{aligned} I_4 &= \int_0^\infty\frac{(\sqrt{q}\ u)^r}{\pi}e^{-i\nu u}\sum_{k=0}^{\infty}\frac{(-qu^2)^k}{k!\ (r+k)!}\left[\psi(k+1)+\psi(r+k+1)\right] \\ &= \sum_{k=0}^{\infty}-\frac{(\sqrt{q})^{(r+2k)}\ \Gamma(r+2k+1)}{\pi\ k!\ (r+q)!\ (i\nu)^{(r+2k+1)}}\left[\psi(k+1)+\psi(r+k+1)\right] \end{aligned} \tag{B.12}$$

Substituting Eqns. B.6,B.7,B.8 and B.12 into Eqn. B.1, the infinite integral will have the form

$$\int_0^\infty e^{-i\nu\cosh\xi} Mc_m^{(4)}(\xi)\sinh\xi\, d\xi = -\sum_{r=0}^{\infty}(-1)^r A_r^{(n)}\left[I_1 - i(I_2 + I_3 - I_4)\right] \tag{B.13}$$

Appendix C

Analytical solution on Infinite integral in Eqn. 3.44.

For simplicity $\cos\zeta$ in Eqn. 3.44 will be replaced by x.

$$f(x) = e^{-i\nu x}\int_{\infty}^{1-x} e^{-i\nu\xi} H_0^{(2)}(\kappa\xi)\, d\xi \tag{C.1}$$

expressing $H_o^{(2)}(z)$ as a linear combination of Bessel functions in the form $H_o^{(2)}(z) = J_o(z) - i\, Y_o(z)$ where

$$\begin{aligned} J_o(z) &= \sum_{m=0}^{\infty} \frac{(-1)^m (z/2)^{2m}}{m!\,\Gamma(m+1)} \\ Y_o(z) &= -\frac{1}{\pi}\sum_{m=0}^{n-1} \frac{(-m-1)!}{m!}\left(\frac{z^2}{4}\right)^m + \frac{2}{\pi} J_o(z)\ln(z/2) - \frac{2}{\pi}\sum_{m=0}^{\infty} \frac{\left(\frac{-z^2}{4}\right)}{m!\; m!}\,\psi(m+1) \end{aligned} \tag{C.2}$$

The first summation of $Y_o(z)$ vanishes as the function order is zero ($n = 0$). Changing the variables of Eqn. C.1 as follows

$$\kappa\xi = z, \quad d\xi = \frac{dz}{\kappa}, \quad ,\xi = 1 - x \to z = \nu(1-x), \quad \xi = \infty \to z = \infty \tag{C.3}$$

Substituting Eqns. C.2 and C.3 into Eqn. C.1 and labeling the resulting term as L_1, L_2 and

L_3, then

$$L_1 = \int_{\kappa(1-x)}^{\infty} e^{-\frac{i\nu z}{\kappa}} \sum_{m=0}^{\infty} \frac{(-1)^m\ (z/2)^{2m}}{m!\ \Gamma(m+1)} = \sum_{m=0}^{\infty} \frac{(-1)^m\ (0.5)^{2m}}{m!\ \Gamma(m+1)} \int_{\kappa(1-x)}^{\infty} e^{-\frac{i\nu z}{\kappa}}\ z^{2m}\ dz$$
$$= \sum_{m=0}^{\infty} \frac{(-1)^m (0.5)^{2m}\ \Gamma(2m+1, \nu(1-x))}{m!\ \Gamma(m+1)\ (\frac{i\nu}{\kappa})^{(2m+1)}} \tag{C.4}$$

$$L_2 = \frac{2}{\pi\ \kappa} \int_{\kappa(1-x)}^{\infty} e^{(\frac{-i\nu z}{\kappa})} \sum_{m=0}^{\infty} \frac{(-1)^m\ (0.5)^{2m}}{m!\ \Gamma(m+1)} \ln\left(\frac{z}{2}\right) dz$$
$$= \frac{2}{\pi\ \kappa} \sum_{m=0}^{\infty} \frac{(-1)^m\ (0.5)^{2m}}{m!\ \Gamma(m+1)} \left[-\ln(2) \int_{\kappa(1-x)}^{\infty} e^{\frac{-i\nu}{\kappa} z} z^{2m} dz + \int_{\kappa(1-x)}^{\infty} e^{\frac{-i\nu}{\kappa} z} z^{2m}\ \ln(z) dz \right] \tag{C.5}$$

Applying appropriate change of variables and with the aid of Leibniz integral rule, the second integral of Eqn. C.5 can be expressed as

$$\int_{\kappa(1-x)}^{\infty} e^{\frac{-i\nu}{\kappa} z} z^{2m}\ \ln(z) dz = \left(\frac{\kappa}{i\nu}\right)^{(2m+1)} \left[\frac{1}{2} \frac{d}{dm}\ \Gamma(2m+1, i\nu(1-x)) + \ln\left(\frac{\kappa}{i\nu}\right) \Gamma(2m+1, i\nu(1-x)) \right] \tag{C.6}$$

Substituting Eqn. C.6 into Eqn. C.5, L_2 have the form

$$L_2 = \frac{2}{\pi\ \kappa} \sum_{m=0}^{\infty} \frac{(-1)^m\ (0.5)^{2m}}{m!\ \Gamma(m+1)}\ \times$$
$$\left[-\ln(2) \left(\frac{i\nu}{\kappa}\right)^{(-2m-1)} + \left(\frac{\kappa}{i\nu}\right)^{(2m+1)} \left(\frac{1}{2} \frac{d}{dm}\ \Gamma(2m+1, i\nu(1-x)) + \ln\left(\frac{\kappa}{i\nu}\right) \Gamma(2m+1, i\nu(1-x)) \right) \right] \tag{C.7}$$

where

$$\frac{d}{dm}\ \Gamma(2m+1, i\nu(1-x)) = 2\times \left[\Gamma(2m+1, i\nu(1-x))\ \ln(i\nu(1-x)) + G^{\,3\ 0}_{2\ 3} \left({}^{1,\,1}_{0,\,0,\,(2m+1)} \middle| i\nu(1-x) \right) \right] \tag{C.8}$$

$$L_3 = \frac{2}{\pi}\sum_{m=0}^{\infty}\frac{\psi(m+1)\ (-0.25)^m}{(m!)^2}\int_{\kappa(1-x)}^{\infty} e^{\frac{-i\nu}{\kappa}\ z} z^{2m} dz = \frac{2}{\pi}\sum_{m=0}^{\infty}\frac{\psi(m+1)\ (-0.25)^m \Gamma(2m+1, \nu(1-x)}{(m!)^2\ (\nu/\kappa)^{(2m+1)}} \tag{C.9}$$

Finally, from Eqns. C.1, C.4, C.7 and C.9 the function $f(x)$ can be expressed as

$$f(x) = e^{-i\nu x}\int_{\infty}^{1-x} e^{-i\nu\xi} H_0^{(2)}(\kappa\xi)\ d\xi\ = \frac{-1}{\kappa} e^{-i\nu x}\ [L_1 - i\ (L_2 - L_3)] \tag{C.10}$$